HAL open science

Simplified and complete phase-field fracture formulations for heterogeneous materials and their solution using a Fast Fourier Transform based numerical method

Xiao Ma, Yang Chen, Modesar Shakoor, Dmytro Vasiukov, Stepan Lomov, Chung Hae Park

To cite this version:

Xiao Ma, Yang Chen, Modesar Shakoor, Dmytro Vasiukov, Stepan Lomov, et al.. Simplified and complete phase-field fracture formulations for heterogeneous materials and their solution using a Fast Fourier Transform based numerical method. Engineering Fracture Mechanics, 2023, 279, pp.109049. 10.1016/j.engfracmech.2023.109049 . hal-03932149

HAL Id: hal-03932149

https://hal.science/hal-03932149v1

Submitted on 10 Jan 2023

HAL is a multi-disciplinary open access archive for the deposit and dissemination of scientific research documents, whether they are published or not. The documents may come from teaching and research institutions in France or abroad, or from public or private research centers.

L'archive ouverte pluridisciplinaire **HAL**, est destinée au dépôt et à la diffusion de documents scientifiques de niveau recherche, publiés ou non, émanant des établissements d'enseignement et de recherche français ou étrangers, des laboratoires publics ou privés.

Simplified and complete phase-field fracture formulations for heterogeneous materials and their solution using a Fast Fourier Transform based numerical method

Xiao Ma[1], Yang Chen[2], Modesar Shakoor*[1], Dmytro Vasiukov[1], Stepan Lomov[3], and Chung Hae Park[1]

[1]IMT Nord Europe, Institut Mines-Télécom, Univ. Lille, Centre for Materials and Processes, F-59000 Lille, France

[2]Materials and Structures Centre, Department of Mechanical Engineering, University of Bath, Claverton Down, Bath, United Kingdom, BA2 7AY

[3]Department of Materials Engineering, KU Leuven, Belgium

January 10, 2023

Abstract

This paper focuses on the numerical implementation of phase-field models of fracture using the Fast Fourier Transform based numerical method. Recent developments in that field rely on the separate solution of a coupled problem where the mechanical equilibrium problem is solved first, and then the phase-field evolution equation. The latter involves a diffusion term which has been simplified in previous

*Corresponding author: modesar.shakoor@imt-nord-europe.fr

works relying on the Fast Fourier Transform based numerical method. This simplification has theoretically no effect for homogeneous materials, but might influence predictions significantly for heterogeneous materials where fracture properties vary between the different components.

In this paper, the influence of this simplification is assessed and a complete formulation is proposed as well as a novel implementation of this formulation using the Fast Fourier Transform based numerical method. The assessment relies on simulations with a material containing two components, one of them being defined as unbreakable by using higher fracture properties. Using the simplified formulation, the presence of an artificial diffusion of damage between the two components is evidenced, and non-zero damage values are observed in the unbreakable component. Although the complete formulation leads to an increase of the number of iterations to solve the phase-field evolution equation, it suppresses completely the diffusion of damage towards the unbreakable component. The two formulations, in fact, lead to identical results when the fracture properties are homogeneous, but the results diverge both in terms of local fracture patterns and global stress-strain relations when the fracture properties contrast increases. This difference is also more pronounced when the regularization length introduced by the phase-field model increases.

Keywords: Fast Fourier Transform (FFT), Phase-field, Damage modeling, Heterogeneous material

1 Introduction

A good comprehension of the failure mechanics of materials requires a deep study on the microscale, especially for heterogeneous materials. One of the study directions of cracks in heterogeneous materials is fracture mechanics, which principally focuses on the crack initiation and propagation. This subject has been extensively studied since the milestone works of Griffith [1] and Irwin [2]. In the work of Griffith, a global energy approach is provided to find quantitative relations between the crack length, the resistance to the crack growth of the materials, and the criterion of crack propagation that regards fracture as a competition between the surface energy of propagation and the elastic energy stored in the bulk material.

Another discipline is Continuum Damage Mechanics of local material properties (CDM). If we look at the microscale, right before the material attains its strength, the macro-crack does not propagate directly. First, there is an accumulation and evolution of local micro-defects, such as micro-cracks and micro-cavities. Due to these micro-defects, the surface for bearing the load reduces. Hence, the material cannot carry the load as before even if the effective macroscopic load increases. From a global point of view, this phenomenon can be regarded as the degradation of local material properties. The degree of material degradation can be described by a continuous parameter d called the damage variable. This variable d varies in the range $[0, 1]$, where 0 means intact state and 1 means fully degraded state.

Phase-field models, one of the branches of CDMs, also utilize a damage variable d to describe the failure state. In the phase-field approach, sharp cracks are regularized as diffusive crack bands by a function of d [3, 4]. On the one hand, the evolution of the phase-field variable itself completely describes the initiation and propagation of cracks in the material. On the other hand, phase-field models are closely related to the variational approach to brittle fracture [5]. This approach enables a simultaneous approximation of the displacement field and the cracks by minimizing the total potential energy of the solid.

Comparisons between gradient-based non-local damage models and the phase-field approach can be found in the literature [6, 7]. These studies show that the two approaches are similiar in terms of equations and solutions. Even some gradient-based damage models have been proposed that tend to be closer to the phase-field model [8]. That is why some researchers consider the phase-field model as a gradient-based non-local damage model. However, as discussed in Refs. [6, 9], their fundamental ideas are different. The gradient-based non-local damage model was proposed to average the local damage field to solve the mesh dependency, while the phase-field model departs from the discontinuous description of a crack, where a distribution function is introduced to smear this discontinuity. For example, the regularization from sharp crack to diffusive crack is not introduced in Ref. [8] even if the final equations are almost the same as in the phase-field approach. More details can be found in the review paper [9].

Compact formulations of the phase-field model can be found in Refs. [10, 11, 12]. These works and others have promoted the variational phase-field models in the engineering community. According to the literature [9, 13], the major characteristics of the phase-field model can be summarized as follows:

- The phase-field model is purely based on energy minimization, and there is no need for a pre-defined crack.
- Multi-cracks merging and branching problems can be solved without additional effort.
- The model can easily be applied in 3D cases, and numerical implementation is straightforward.
- The model is non-local and intrinsically avoids mesh dependency.

The phase-field approach, hence, has gained increased attention among the damage modeling techniques. Many applications of this approach can be found in the recent literature. Espadas-Escalante analyzed the fracture behavior of fiber-reinforced composites on the microscopic scale [14]. In Ref. [15], a phase-field model has been applied to study cracks in concrete materials. For a multi-phase system, phase-field models can be combined with other phase-field [15] or cohesive zone models [16] to study the interface debonding problem.

Although numerical methods based on the phase-field approach is generally considered mesh independent, a condition on element size must be ensured. It has been proven in Ref. [10] that the characteristic length of the phase-field model needs to be twice larger than the element size of the fractured zone. In this context, especially for 3D simulations, conventional finite element solvers can be cumbersome and hence require an efficient parallel implementation to extend the computational limits [17]. There is a demand for massive parallelization in complex microstructure cases to get a reasonable computational time.

The Fast Fourier Transform (FFT)-based method was initially proposed by Moulinec and Suquet [18, 19, 20] in 1994 as a voxel-based methodology that does not need stiffness matrix assembling, unlike conventional finite element solvers. In the FFT-based method, the

local strain tensor is calculated by a convolution product with a fourth-rank Continuous Green Operator (CGO) and a polarization term. The convolution product is transformed into a simple multiplication in Fourier space. The multiplication of the polarization term and the CGO are local operations that can be easily parallelized [21]. The FFT operation itself is not a local operation but efficient parallel implementations are available (such as FFTW [22]). Consequently, large-scale simulations based on full-resolution images can be performed with the FFT-based method. Since its proposition, FFT-based methods have been improved and applied to investigate a wide range of physical phenomena in heterogeneous materials [21, 23].

As it was shown in Refs. [24, 25], the combination of the FFT method with the phase-field model for fracture problems can be attractive. However, a fundamental issue must be taken into account for heterogeneous materials, which is the main subject discussed in this paper.

When studying fracture problems, a model can often be categorized by the degree of isotropy and homogeneity. Isotropic models, in our studies, have two main families of properties that can help to describe the degree of homogeneity: elastic properties, such as Young's modulus (E), and damage properties, such as critical energy release rate (G_c). In our recent studies, if the damage properties are homogeneous, the solver in Ref. [24] works well no matter the homogeneity degree on elastic properties. However, if the damage properties become heterogeneous, the results often show non-physical damage diffusion between phases. This is the main topic that will be discussed in the present paper, and the word *heterogeneous* herein is mainly linked to the damage properties.

Based on the paper of Jeulin [26], due to the fact that the G_c values are not constant, one term in the phase-field equation has been omitted in Ref. [24] for heterogeneous materials. Although various works have adopted a heterogeneous setting for material fracture properties, it is still not fully clear whether such heterogeneity can be justified, for which rigorous discussions are seldom in the literature. A recent work [27] discussed this aspect using 1D heterogeneous bars.

The present work focuses on Miehe's initial formulation of the phase-field approach

[10, 11], although the readers are to be aware that numerous improvements and extensions have been proposed in the later literature. For the sake of brevity, in the subsequent text, the algorithm used in Ref. [24] will be called the simplified formulation, and the modified algorithm after adding the heterogeneity correction will be called the complete formulation. Note that a recent paper [25] utilizes a multi-phase-field system for heterogeneous mediums, which may also be able to solve the mentioned diffusion issue, but it is not the scope of this paper.

The paper is organized as follows: first, a brief review of Miehe's phase-field model, on which this paper will focus, is presented in Sec. 2. Then, the implementation of the complete formulation in the FFT-based solver is presented in Sec. 3. Third, several numerical experiments are carried out in Sec. 4 to compare the difference between simplified and complete formulations. Finally, Sec. 5 presents general conclusions.

2 Review of Miehe's phase-field model

The starting point of Miehe's phase-field model [10] is smearing the sharp crack topology by a diffusive crack band, as illustrated in Fig. 1. The crack is smeared using the exponential function

$$d\left(x\right) = \exp\left(-\frac{|x|}{l_c}\right). \tag{1}$$

The solid Ω with a crack set Γ (or Γ_l) is presented in Fig. 1. The conventional sharp crack is shown in Fig. 1(a) and the diffusive crack used in phase-field is shown in Fig. 1(b). The damage variable d represents the local damage state with $d = 1$ for fully damaged material and $d = 0$ for the intact state.

Since the model in Fig. 1(a) possesses a sharp crack, we will get the delta function shown in the yellow window if we draw the evolution of d along the AB line. This contrasts with the diffusive crack presented in Fig. 1(b), where the crack is approximated as a crack band characterized by a length parameter l_c.

The influence of l_c values on the damage band diffusion is presented in Fig. 1(c). The smaller l_c is, the narrower the crack band is. The curves in Fig. 1(c) all satisfy that $d = 1$

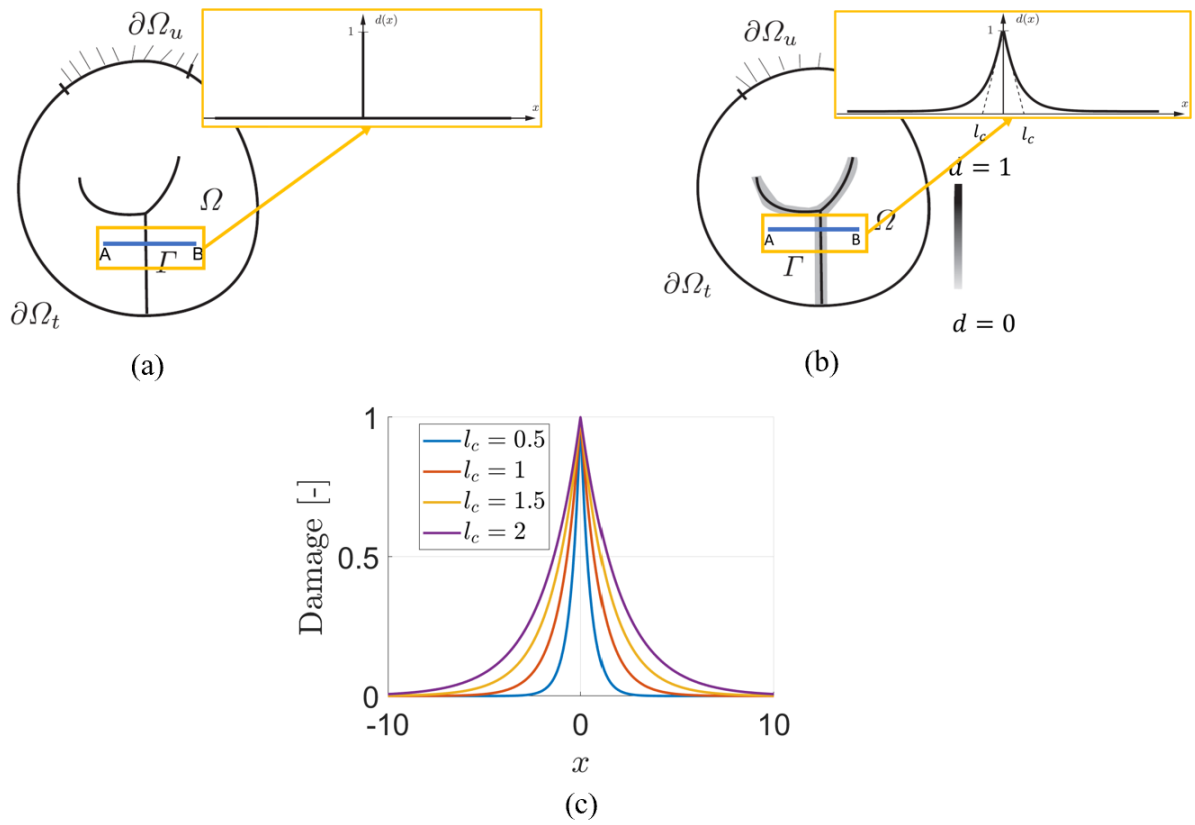

Figure 1: A solid body Ω with the crack set Γ (or Γ_l): (a) sharp cracks and (b) approximated diffuse crack bands. (c) Illustration of diffusive damage profile of a crack at $x = 0$ for various length parameters l_c.

when $x = 0$, and that d vanishes far away from $x = 0$.

Looking at Miehe's formulation, in a 1D case, it can be easily verified that the diffusive crack function in Eq. (1) is a solution to the following ordinary differential equation (ODE)

$$\frac{1}{l_c} d\left(x\right) - l_c d''\left(x\right) = 0, \tag{2}$$

subjected to the Dirichlet-type boundary conditions: $d\left(x = 0\right) = 1$ and $d\left(x = \pm\infty\right) = 0$. On the one side, in consistence with the variational approach to fracture, the crack surface function can be obtained from the minimization of the crack surface that yields the ODE shown in Eq. (2):

$$d\left(x\right) = \arg\left\{\inf\left[\Gamma_l\right]\right\},$$

with Γ_l expressed as

$$\Gamma_l(d) = \int_{-\infty}^{+\infty} \frac{1}{2}\left[\frac{1}{l_c}d^2 + l_c\left(d'\right)^2\right]\mathrm{d}x = \int_{-\infty}^{+\infty} \gamma \mathrm{d}x,$$

where γ is the crack surface density. The extension to a higher dimension is straightforward:

$$\gamma(d, \nabla d) = \frac{1}{2}\left[\frac{1}{l_c}d^2 + l_c\left(\nabla d\right)^2\right], \tag{3}$$

where d' has been replaced by ∇d.

On the other side, the phase-field is also in line with Griffith's theory [1]. In this energetic approach, the damage evolution and crack propagation result from the competition between the bulk energy stored in the body and the energy dissipation from the opening of the crack surface. From this point of view, in quasi-static loading, the total energy Π can be expressed as:

$$\Pi := \Phi_s + \Phi_d - P, \tag{4}$$

where Φ_s is the strain energy stored in the cracked body, Φ_d is the energy dissipated for opening the crack surface, and P is the external loading. As illustrated in Fig. 1(c), we consider a domain $\Omega \subset \mathbb{R}^n$ $(n = 1, 2, 3)$ which contains a diffusive crack set Γ_l with $\Gamma_l \subset \mathbb{R}^{n-1}$ and is under a volumetric loading by a body force f^*, a displacement u^* on the boundary $\partial\Omega_u$, and a surface force t^* on the complementary boundary $\partial\Omega_t$ $(\partial\Omega = \partial\Omega_u \bigcup \partial\Omega_t)$, where the symbol $()^*$ means a prescribed term. A detailed formulation of the components in Eq. (4) is presented as follows:

$$\Phi_s = \int_\Omega \varphi(\varepsilon, \Gamma_l)\,\mathrm{d}\Omega = \int_\Omega g(d)\,\varphi_0(\varepsilon)\,\mathrm{d}\Omega, \tag{5a}$$

$$\Phi_d = \int_{\Gamma_l} G_c \mathrm{d}\partial\Omega \approx \int_\Omega G_c \gamma \mathrm{d}\Omega, \tag{5b}$$

$$P = \int_\Omega f^* \cdot u \mathrm{d}\Omega + \int_{\partial\Omega_t} t^* \cdot u \mathrm{d}\partial\Omega + \int_{\partial\Omega_u} (\sigma \cdot n) \cdot u^* \mathrm{d}\partial\Omega, \tag{5c}$$

where φ is the elastic strain energy density stored in the cracked body, g is the energetic degradation function, φ_0 is the initial strain energy, ε is the strain tensor, G_c is the critical energy release rate, σ is the stress tensor and n is the outward normal vector.

The displacement field and the crack set can be solved by minimizing the total energy with the variational approach [4]:

$$\left(u(t), \Gamma_l(t)\right) = \arg\left\{\min\left[\Pi\left(u, \Gamma_l\right)\right]\right\}, \tag{6}$$

under the constraint of irreversibility, which is stated as $\dot{\Gamma}_l \geq 0$, and under the boundary conditions: $u(x) = u^*$ at $\partial\Omega_u$, and $\sigma \cdot n = t^*$ at $\partial\Omega_t$. Assuming a zero body force, the detailed expression of Eq. (4) is

$$\Pi(u,d) = \int_\Omega \varphi(\varepsilon(u), d)\,\mathrm{d}\Omega + \int_\Omega G_c \gamma(d, \nabla d)\,\mathrm{d}\Omega - \int_{\partial\Omega_t} t^* \cdot u \mathrm{d}\partial\Omega - \int_{\partial\Omega_u} (\sigma \cdot n) \cdot u^* \mathrm{d}\partial\Omega. \quad (7)$$

Eq. (7) is then rewritten in the variational form for determining the displacement and phase-field (u, d):

$$\begin{aligned} \delta\Pi(u,d) = \; & \textstyle\int_\Omega \sigma : \delta\varepsilon \mathrm{d}\Omega + \int_\Omega g'(d)\delta d \varphi_0(\varepsilon)\,\mathrm{d}\Omega \\ & + \textstyle\int_\Omega G_c \left(\frac{\partial\gamma}{\partial d}\delta d + \frac{\partial\gamma}{\partial\nabla d}.\delta\nabla d\right)\mathrm{d}\Omega - \int_{\partial\Omega_t} t^* \cdot \delta u \mathrm{d}\partial\Omega, \end{aligned} \quad (8)$$

where $\sigma = \frac{\partial\varphi}{\partial\varepsilon}$ denotes the Cauchy stress, and $\delta u = 0$ for $\forall x \in \partial\Omega_u$. In general, Eq. (8) can be divided into two parts $\delta\Pi(u,d)^{P1}$ and $\delta\Pi(u,d)^{P2}$. The first one is the mechanical part without damage that is written as follows:

$$\delta\Pi(u,d)^{P1} = \int_\Omega \sigma : \delta\varepsilon \mathrm{d}\Omega - \int_{\partial\Omega_t} t^* \cdot \delta u \mathrm{d}\partial\Omega.$$

Regarding $\delta\Pi(u,d)^{P2}$, it can be written as:

$$\delta\Pi(u,d)^{P2} = \int_\Omega g'(d)\,\delta d \varphi_0(\varepsilon)\,\mathrm{d}\Omega + \int_\Omega \frac{G_c}{l_c} d\delta d \mathrm{d}\Omega + \int_\Omega G_c l_c \nabla d.\nabla\delta d \mathrm{d}\Omega. \quad (9)$$

Applying the divergence theorem, Eq. (9) would yield

$$\begin{aligned} \delta\Pi(u,d)^{P2} = \int_\Omega g'(d)\,\delta d \varphi_0(\varepsilon)\,\mathrm{d}\Omega + \int_\Omega \frac{G_c}{l_c} d\delta d \mathrm{d}\Omega - \int_\Omega \nabla \cdot (G_c l_c \nabla d)\,\delta d \mathrm{d}\Omega + \\ \int_{\partial\Omega} (G_c l_c \nabla d \delta d) \cdot n \mathrm{d}\partial\Omega. \end{aligned} \quad (10)$$

The surface integral vanishes by considering the crack boundary condition: $\nabla d(x) \cdot n(x) = 0$. Thus, we have:

$$\delta\Pi(u,d)^{P2} = \int_\Omega g'(d)\,\delta d \varphi_0(\varepsilon)\,\mathrm{d}\Omega + \int_\Omega \frac{G_c}{l_c} d\delta d \mathrm{d}\Omega - \int_\Omega \nabla \cdot (G_c l_c \nabla d)\,\delta d \mathrm{d}\Omega. \quad (11)$$

Since the solution of the crack set, the damage variable herein, is a stationary point of the energy functional, the local damage evolution equation of the phase-field can be written in strong form as:

$$g'(d)\,\varphi_0(\varepsilon) + \frac{G_c}{l_c} d - \nabla \cdot (G_c l_c \nabla d) = 0, \quad (12)$$

when $\delta d > 0$. In the case of homogeneous medium, the G_c and l_c are constant. Thus, $\nabla \cdot (G_c l_c \nabla d) = G_c l_c \Delta d$, and the damage evolution function can be rewritten as:

$$g'(d)\,\varphi_0(\varepsilon) + \frac{G_c}{l_c} d - G_c l_c \Delta d = 0, \tag{13}$$

In Ref. [24], Eq. (13) was applied. However, in the case of heterogeneous medium, G_c and l_c are functions of x for $x \in \Omega$. Thus, these two parameters cannot be directly put outside the divergence operation, and Eq. (12) should be adopted. Comparing Eq. (13) with Eq. (12),

$$\nabla \cdot (G_c l_c \nabla d) = \nabla (G_c l_c) \cdot \nabla d + G_c l_c \Delta d. \tag{14}$$

That means the term $(\nabla (G_c l_c) \cdot \nabla d)$ was omitted in Ref. [24]. This is the reason why the phase-field in Ref. [24] is called the simplified formulation, and the phase-field presented in this work, using Eq. (13), is called the complete formulation. Two particular situations should be considered for the gradient of the fracture parameters $\nabla (G_c l_c)$: (i) a multiphase material with homogeneity inside each phase, and (ii) a single-phase material with continuously varying property (for instance, a functionally-graded material). In situation (i), the gradient $\nabla (G_c l_c)$ is non-zero only at the interfaces between different phases; whereas it is non-zero everywhere in situation (ii). The analyses presented in this work focus on situation (i), which is more often encountered in engineering problems.

For an isotropic elastic body, the initial free energy density in Eqs. (12) and (13) can be expressed as:

$$\varphi_0(\varepsilon) = \frac{1}{2}\lambda tr^2(\varepsilon) + \mu \varepsilon : \varepsilon \tag{15}$$

where λ and μ represent the Lamé coefficients of the material. In order to activate the damage evolution only under tension, a split of the initial strain energy into tensile and compressive parts is necessary under complex loading conditions.

In the work of Miehe [10, 11], a spectral decomposition of the strain tensor has been applied in order to fully distinguish the tensile and compressive strains:

$$\varepsilon = \sum_{n=1}^{3} \varepsilon_n p_n \otimes p_n = \varepsilon_+ + \varepsilon_- \tag{16}$$

where ε_n and p_n denote the eigenvalues and eigenvectors of the strain tensor, respectively. The operator $\otimes$ denotes the outer product of two vectors. Note that ε_+ and ε_- represent

the tension and compression parts of the strain tensor, respectively:

$$\varepsilon_+ = \sum_{n=1}^{3} \langle \varepsilon_n \rangle_+ p_n \otimes p_n, \quad \varepsilon_- = \sum_{n=1}^{3} \langle \varepsilon_n \rangle_- p_n \otimes p_n \tag{17}$$

with the bracket operators $\langle x \rangle_+ = \frac{x+|x|}{2}$, and $\langle x \rangle_- = \frac{x-|x|}{2}$.

Miehe's spectral decomposition can be performed with the help of fourth-order projection tensors, $\mathbb{P}_+$ and $\mathbb{P}_-$, which are shown as follows:

$$\varepsilon_+ = \mathbb{P}_+ : \varepsilon, \qquad \varepsilon_- = \mathbb{P}_- : \varepsilon, \quad \text{and} \quad \mathbb{P}_+ + \mathbb{P}_- = \mathbb{I}, \tag{18}$$

where $\mathbb{I}$ denotes the fourth-order identity tensor. As detailed in Ref. [28] and Appendix A of Ref. [24], the calculation of the projection tensors is mainly based on the eigenvectors (w_1, w_2, w_3) and the eigenvalues (v_1, v_2, v_3) of ε:

$$\mathbb{P}_+ = W^T S W, W = \begin{pmatrix} w_{11} & w_{12} & w_{13} \\ w_{21} & w_{22} & w_{23} \\ w_{31} & w_{32} & w_{33} \end{pmatrix}, S = \begin{pmatrix} s_1 & 0 & 0 \\ 0 & s_2 & 0 \\ 0 & 0 & s_3 \end{pmatrix}, s_i = \begin{cases} 1, & v_i > 0, \\ 0, & v_i \leq 0. \end{cases} \tag{19}$$

The tensile and compressive part of the initial strain energy can then be expressed as:

$$\varphi_0^{\pm} = \frac{1}{2}\lambda \left(\langle tr\left(\varepsilon\right) \rangle_{\pm} \right)^2 + \mu \varepsilon_{\pm} : \varepsilon_{\pm}. \tag{20}$$

As damage only affects the tension part, the stress tensor can be defined as:

$$\sigma = g\left(d\right) \left[\lambda \langle tr\left(\varepsilon\right) \rangle_+ I + 2\mu \varepsilon_+ \right] + \left[\lambda \langle tr\left(\varepsilon\right) \rangle_- I + 2\mu \varepsilon_- \right], \tag{21}$$

with I the identity matrix.

Damage models should reflect the physics, where a fully damaged material cannot be damaged further, and the damage state cannot be recovered. Consequently, the boundedness $d \in [0, 1]$ and irreversibility condition $\dot{d} \geq 0$ should be met. For Miehe's model, the boundedness $d \in [0, 1]$ is dealt with using a so-called history field ($\mathcal{H}$) of maximum positive initial strain energy that replaces φ_0 in Eqs. (12) and (13). This history field is given as:

$$\mathcal{H}\left(x, t_n\right) := \max_{0 \leq t \leq t_n} \left[\varphi_0^+ \left(x, t\right) \right]. \tag{22}$$

Thus, Eq. (12) should rewritten as follows:

$$g'(d)\,\mathcal{H} + \frac{G_c}{l_c} d - \nabla \cdot (G_c l_c \nabla d) = 0, \tag{23}$$

as well as Eq. (13), which can be reexpressed as:

$$g'(d)\,\mathcal{H} + \frac{G_c}{l_c} d - G_c l_c \Delta d = 0. \tag{24}$$

Note that most studies using this model rely on Eq. (24) and a finite element solver. The weak form on which the finite element method is based implies an integration by parts which eliminates the divergence operator from the phase-field evolution equation. It does not make sense, therefore, to distinguish between a simplified and a complete formulation for finite element solvers. The following discussions are specific to FFT-based solvers. It is possible that they could be generalized to finite difference solvers as well but it is outside of the scope of our work.

3 Implementation of the complete formulation into an FFT-based solver

In the work of Chen et al. [24], a fixed-point algorithm was adopted to solve the phase-field governing equation, and the mechanical part was solved separately. A weak coupling scheme was applied to bridge the phase-field and mechanical parts. This method is relatively straightforward to implement. Thus, the same algorithm is adopted in this work and is not detailed. It is reminded that periodic boundary conditions are intrinsic to FFT-based methods, and that those methods can only rely on regular (Cartesian) grids composed of hexahedral elements that we coin voxels. All fields (including the strain field, the stress field and the phase-field) are discretized as voxel-wise constant variables. More details can be found in Ref. [24].

Due to the complexity of the complete formulation, the solving procedure is slightly more intricate and is hence detailed in the following. The main ideas are inspired from the work of Jeulin [26].

First, a term $Q(x)$,

$$Q(x) = G_c(x) l_c(x), \tag{25}$$

is introduced to describe the multiplication of G_c and l_c. A fluctuation term $\tilde{Q}(x)$ is then introduced, and Eq. (25) can be reexpressed as:

$$Q(x) = Q_0 + \tilde{Q}\left(x\right), \tag{26}$$

where

$$Q_0 = \frac{\max_{x\in\Omega}\left(Q\left(x\right)\right) + \min_{x\in\Omega}\left(Q\left(x\right)\right)}{2}. \tag{27}$$

Therefore, Eq. (23) can be rewritten as:

$$-2\left(1-d\left(x\right)\right)\mathcal{H}\left(x\right) + \frac{G_c\left(x\right)}{l_c\left(x\right)}d\left(x\right) - \nabla\cdot\left(Q_0\nabla d\left(x\right)\right) - \nabla\cdot\left(\tilde{Q}\left(x\right)\nabla d\left(x\right)\right) = 0, \tag{28}$$

with

$$g(d) = \left(1-d\right)^2, \quad g'(d) = -2\left(1-d\right).$$

In the weak coupling scheme, the damage variable at time t_{n+1}, denoted by $d^{t_{n+1}}$, is calculated based on the history field at time t_n, denoted by $\mathcal{H}^{t_n}$. This $\mathcal{H}^{t_n}$ remains constant when solving the damage variable $d^{t_{n+1}}$. Since Q_0 is constant over the domain, Eq. (28) gives:

$$\left(\frac{G_c\left(x\right)}{l_c\left(x\right)} + 2\mathcal{H}^{t_n}\left(x\right)\right)d^{t_{n+1}}\left(x\right) - Q_0\Delta d^{t_{n+1}}\left(x\right) = 2\mathcal{H}^{t_n}\left(x\right) + \nabla\cdot\left(\tilde{Q}\left(x\right)\nabla d^{t_{n+1}}\left(x\right)\right). \tag{29}$$

Setting

$$A^{t_n}(x) = \frac{G_c\left(x\right)}{l_c\left(x\right)} + 2\mathcal{H}^{t_n}\left(x\right), \tag{30a}$$

$$B^{t_n}(x) = 2\mathcal{H}^{t^n}(x), \tag{30b}$$

$$D^{t_{n+1}}(x) = \nabla\cdot\left(\tilde{Q}\left(x\right)\nabla d^{t_{n+1}}\left(x\right)\right), \tag{30c}$$

Eq. (29) can be rewritten as:

$$A^{t_n}(x)d^{t_{n+1}}\left(x\right) - Q_0\Delta d^{t_{n+1}}\left(x\right) = B^{t_n}(x) + D^{t_{n+1}}(x). \tag{31}$$

Polarizing A^{t_n} with

$$A_0^{t_n} = \frac{\max_{x\in\Omega}\left(A^{t_n}(x)\right) + \min_{x\in\Omega}\left(A^{t_n}\left(x\right)\right)}{2},$$

Eq. (31) gives

$$A_0^{t_n}d^{t_{n+1}}\left(x\right) - Q_0\Delta d^{t_{n+1}}\left(x\right) = \tau\left(x\right), \tag{32}$$

with

$$\tau(x) = B^{t_n}(x) - \left(A^{t_n}(x) - A_0^{t_n}\right) d^{t_{n+1}}(x) + D^{t_{n+1}}(x).$$

In Fourier space, the Laplacian operation in Eq. (32) can be easily transformed into a multiplication with frequency vector ξ, which gives:

$$\mathcal{F}\left[\Delta d^{t_{n+1}}\right](\xi) = -(\xi \cdot \xi)\widehat{d}^{t_{n+1}},$$

where $\mathcal{F}[-]$ denotes the Fourier transform operation, and $\widehat{[-]}$ describes components in Fourier space. Hence, at a given fixed-point iteration i, a new damage field can be solved from Eq. (32):

$$\widehat{d}_{i+1}^{t_{n+1}} = \frac{\widehat{\tau}_i}{A_0^{t_n} + Q_0(\xi \cdot \xi)}. \tag{33}$$

The fixed-point algorithm can be summarized as follows:

$$\begin{array}{lc}
\text{Initialization, if } t_n = 0: & \\
(a_0) & d^0(x) = 0 \\
(b_0) & \text{Calculate } \tilde{Q}(x) \text{ and } Q_0 \\
 & \\
\text{if } t_n \neq 0: & \\
(a_1) & A^{t_n}(x) \text{ is known and } A_0^{t_n} \text{ is known} \\
(b_1) & B^{t_n}(x) \text{ is known and } d^{t_n}(x) \text{ is known} \\
(c_1) & \text{Calculate } D_{i=0}^{t_{n+1}}(x), \text{ and } \tau_{i=0}(x) \\
 & \\
\text{Time } t_{n+1}: & \\
 & \text{While convergence criterion is not met:} \\
(a_2) & \widehat{\tau}_i = \mathcal{F}[\tau_i],\ i^{th} \text{ iteration} \\
(b_2) & \widehat{d}_{i+1}^{t_{n+1}}(\xi) = \frac{\widehat{\tau}_i(\xi)}{A_0^{t_n} + Q_0 \cdot (\xi \cdot \xi)} \\
(c_2) & d_{i+1}^{t_{n+1}}(x) = \mathcal{F}^{-1}[\widehat{d}_{i+1}^{t_{n+1}}](x) \\
(c_2) & \text{Calculate } D_{i+1}^{t_{n+1}}(x), \text{ and } \tau_{i+1}(x) \\
(d_2) & e = ||d_{i+1}^{t_{n+1}} - d_i^{t_{n+1}}||_2 \leq e^{\text{crit}}, \text{ Convergence check}
\end{array} \tag{34}$$

The calculation of $D^{t_{n+1}}$ is performed in Fourier space because the derivation operation in real space is a simple multiplication in Fourier space:

$$D^{t_{n+1}} = \mathcal{F}^{-1}\left(J \cdot \xi \cdot F\left(\tilde{Q} \cdot \mathcal{F}^{-1}\left(J \cdot \xi \cdot \widehat{d}^{t_{n+1}}\right)\right)\right) \tag{35}$$

where $J = \sqrt{-1}$. Compared to the simplified formulation, the complete formulation adds one more Fourier transform and two more inverse transforms.

Compared to Ref. [11], the viscous term, which was introduced for numerical stabilization for a rate-independent material, is not presented in this work. This is because from our experience, the viscous regularization has never really been needed in practice, as the solution of the phase-field problem usually converges well with Anderson's acceleration technique.

Concerning the convergence criterion, in this work, the one for phase-field problem is set as $||d_{i+1} - d_i||_2 \leq e^{\text{crit}} = 1.00 \times 10^{-6}$. The convergence criterion of the mechanical problem is set as $\frac{\left(\langle||\nabla.\sigma_{i+1}||_2^2\rangle\right)^{\frac{1}{2}}}{||\langle\sigma_{i+1}\rangle||_2} \leq e^{\text{crit}}_{\text{meca}} = 1.00 \times 10^{-4}$, where the brackets around a variable denote a volume average over the domain, for instance $\langle\sigma\rangle = \frac{1}{|\Omega|}\int_\Omega \sigma \mathrm{d}\Omega$. The convergence criteria and the tolerance values are the same as in Ref. [24].

To speed up the convergence of the fixed-point algorithm, Anderson's acceleration algorithm is incorporated in this work. This technique has been implemented in the software AMITEX [29], which is also the main environment that is chosen for this work. Note that the grid is distributed in AMITEX, which means all operations are solved in parallel including the mechanical and phase-field solvers. The principal idea of Anderson's acceleration algorithm is to give an improved solution based on the four previous iterations. A detailed description of this algorithm can be found in Ref. [21].

Fig. 2 presents a detailed flowchart of the implementation of the complete formulation. For comparison, the flowchart of the simplified formulation can be found in Appendix B of Ref. [24]. As illustrated in Fig. 2, the history field at time t_n is applied to calculate the damage field at time t_{n+1}. Thus, a sufficiently fine time step is required. According to results from Ref. [24], a time step $\delta\langle\varepsilon\rangle = 5.00 \times 10^{-7}$ is utilized in the present work.

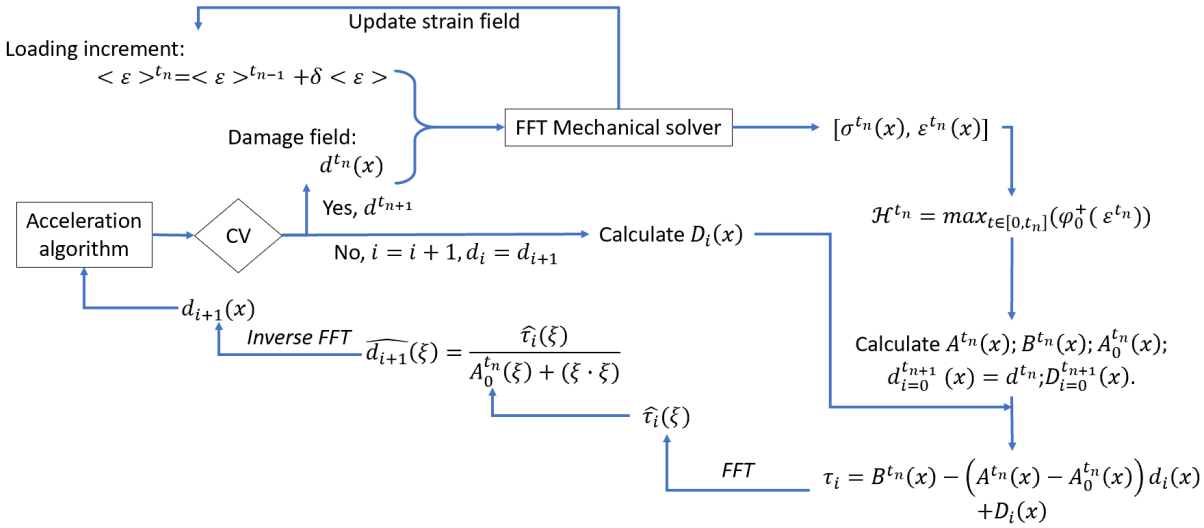

Figure 2: The flow chart of the implementation of the complete formulation into an FFT solver. CV means convergence check.

As for the FFT solver, the work in Ref. [24] utilized a modified discrete Green operator, the so-called rotated-scheme proposed by Willot [30]. In the present work, the basic-scheme, the original method proposed by Moulinec and Suquet [19], is adopted for the mechanical and phase-field problems for both simplified and complete formulations. A detailed description and quantitative studies of these two schemes can be found in Ref. [23].

4 Numerical experiments and discussions

4.1 Unit-cell model with two half fibers on the borders

First, a unit-cell model with two half fibers on the borders is analyzed (as shown in Fig. 3). The model size is 2.00×10^{-2} mm with a fiber volume fraction of $V_f = 0.55$, and an inter-fiber distance $l_f = 3.29 \times 10^{-3}$ mm, while one voxel size is used in the thickness ($z-$ direction). According to our previous work [23], for a unit-cell composite model, a resolution of $N = 225$ is sufficient to get a proper response. This is also used in the present work, which gives a voxel size of $h = 8.89 \times 10^{-5}$ mm.

The blue part is the fiber for which the material is E-glass with properties [24]: $E_f =$

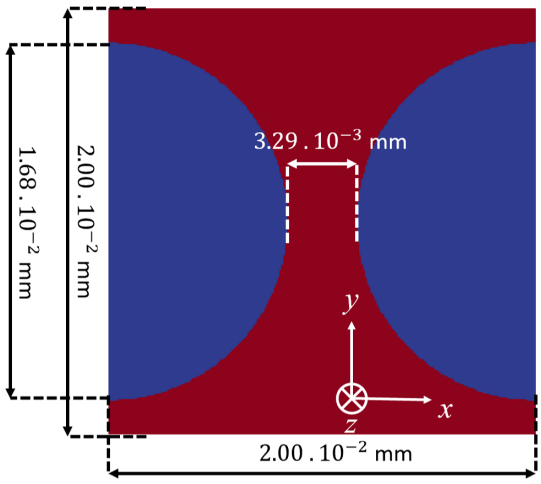

Figure 3: The composite model with two half fibers on the borders (blue part: fiber; red part: matrix).

7.40×10^1 GPa, $\nu_f = 0.2$, and $G_c^f = 6.00 \times 10^1\,\mathrm{N\,mm^{-1}}$. The red part is the matrix for which the material is Epoxy with properties [14]: $E_m = 4.65$ GPa, $\nu_m = 0.35$, and $G_c^m = 9.60 \times 10^{-4}\,\mathrm{N\,mm^{-1}}$.

In this series of simulations, the value of l_c varies from 5.40×10^{-4} mm to 3.30×10^{-3} mm while the inter-fiber distance is fixed. The minimum value of l_c satisfies Miehe's criterion, which states that $l_c^{min}/h = 6.00 > 2.00$, where h denotes the voxel size.

In the following, the model in Fig. 3 is subjected to a macroscopic strain along the x-direction (transverse direction) with a time step $\delta\langle\varepsilon_{xx}\rangle = 5.00 \times 10^{-7}$ until the final failure while stress-free conditions are imposed in the other directions ($\langle\sigma_{yy}\rangle = \langle\sigma_{zz}\rangle = \langle\sigma_{xy}\rangle = \langle\sigma_{xz}\rangle = \langle\sigma_{yz}\rangle = 0$). These mixed-type loading conditions are applied by using the method presented in [31]. Due to stress-free boundaries, Poisson's effect is active during loading.

4.1.1 Simplified formulation

Considering the fiber is much stiffer than the matrix, and the G_c value of fiber is much larger than that of the matrix, a logical hypothesis is that the crack would occur in the matrix, and the damage state in the fiber would be close to null in the present case. However, Table. 1 implies a converse condition: the maximum damage in the fiber is not null for all tests and rises with increasing the l_c. One may argue that this is the intrinsic

feature of Miehe's model, which lacks an elastic regime. We demonstrate in the following that this should not be the only reason.

$l_c(\times 10^{-4})$ mm	5.40	8.10	13.00	22.00	33.00
d_f^{max}	0.15	0.24	0.38	0.56	0.68

Table 1: The maximum damage d_f^{max} in the fiber at the final failure state for various l_c values and for the two half fibers model.

Fig. 4 shows the local damage fields. When $l_c = 5.40 \times 10^{-4}$ mm, there is an apparent distinction between matrix and fibers. In contrast, this transition becomes smeared for $l_c = 3.30 \times 10^{-3}$ mm.

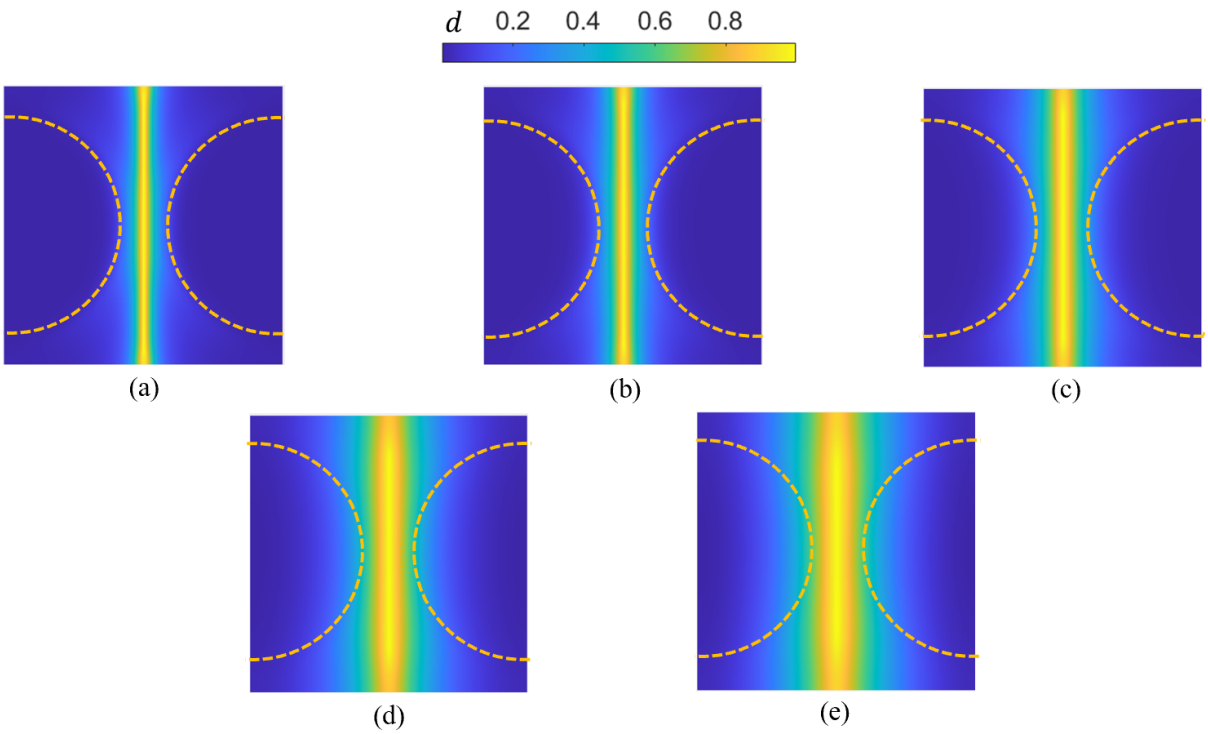

Figure 4: The local damage fields at the final failure state for different l_c values and for the two half fibers model: (a) 5.40×10^{-4} mm; (b) 8.10×10^{-4} mm; (c) 1.30×10^{-3} mm; (d) 2.20×10^{-3} mm; (e) 3.30×10^{-3} mm. The orange dashed lines are the fiber contours.

Then local damage profiles along the center line for different l_c values are plotted in Fig. 5. As shown in the figure, whatever the l_c values, the damage profiles are so smooth

that we can not even distinguish the transition between matrix and fibers. Thus, another hypothesis can be proposed: the damage state in fibers is not physical damage. They are mainly due to the diffusion of matrix damage into the fibers.

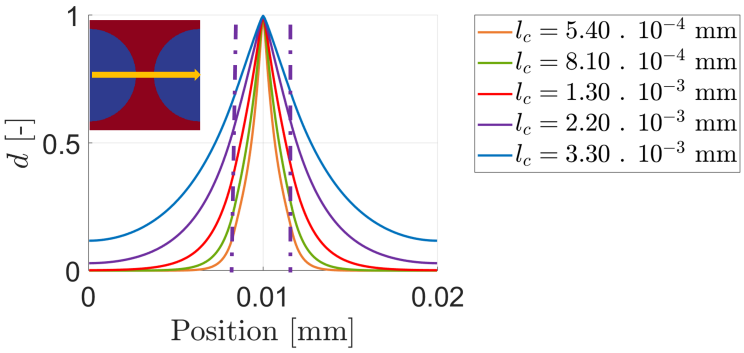

Figure 5: The damage profiles along the center line for different l_c values and for the two half fibers model. The purple dashed lines are boundaries between fibers and matrix.

To verify the proposed hypothesis, higher critical energy release rate values G_c^f are tested for the fiber to check whether they can reduce the damage in fibers. The present work takes two groups of l_c values for tests ($l_c = 1.30 \times 10^{-3}$ mm and 3.30×10^{-3} mm). For each group, G_c^f values vary from 6.00×10^1 N mm^{-1} to 9.00×10^{20} N mm^{-1}. Such unrealistically high values are used to justify the proposed hypothesis. Results are plotted in Fig. 6. When G_c^f increases to a very high value, we would logically expect the damage variable in the fibers to decrease. However, as seen in the figure, whatever the G_c^f values, the macroscopic stress-strain curves do not change for the two test groups, and the damage profiles remain stable. This phenomenon confirms that the damage in the fiber is artificially caused by the diffusion of matrix damage to the fiber side.

4.1.2 Complete formulation

In this part, the same geometric model, materials and settings are adopted for testing the complete formulation. The results are shown in Figs. 7, 8 and 9. Fig. 7 indicates that the maximum damage state in the fiber is negligible after applying the complete formulation.

In Fig. 8, the boundaries between fibers and matrix can be easily identified for all l_c

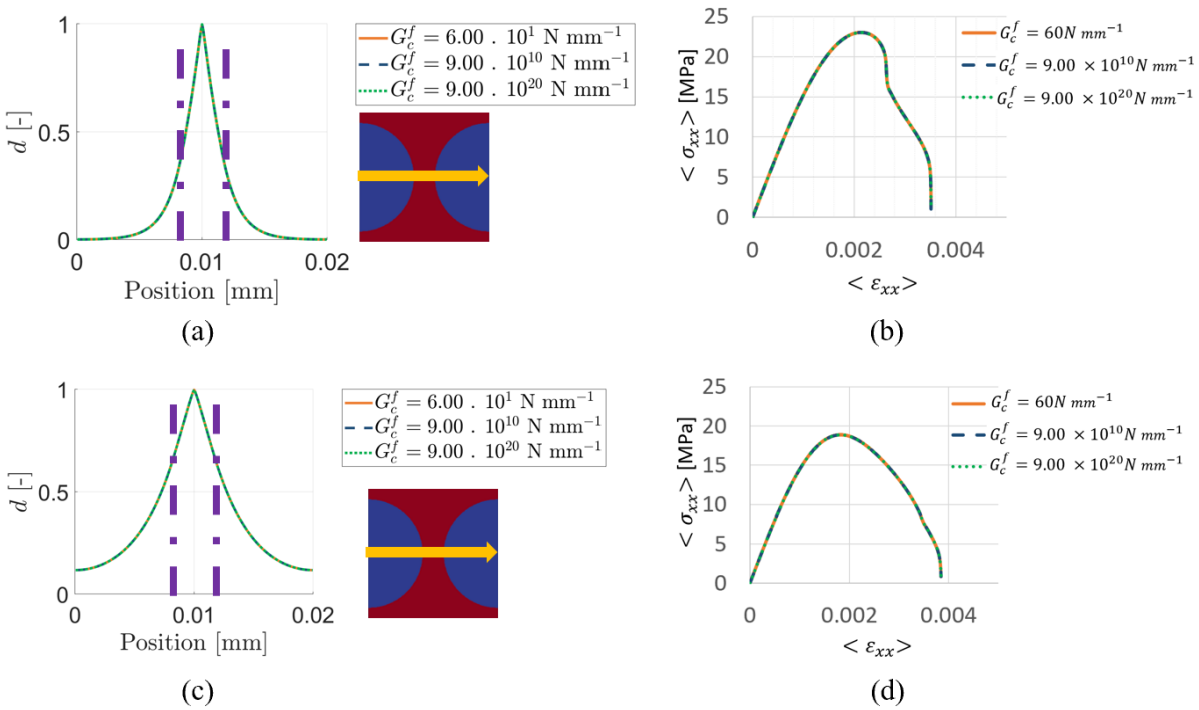

Figure 6: The local damage profiles and macro-level stress-strain relations for different G_c^f values and for the two half fibers model: (a), (b): results for $l_c = 1.30 \times 10^{-3}$ mm; (c), (d): results for $l_c = 3.30 \times 10^{-3}$ mm. The purple dashed lines are boundaries between fibers and matrix, and different curves are superimposed.

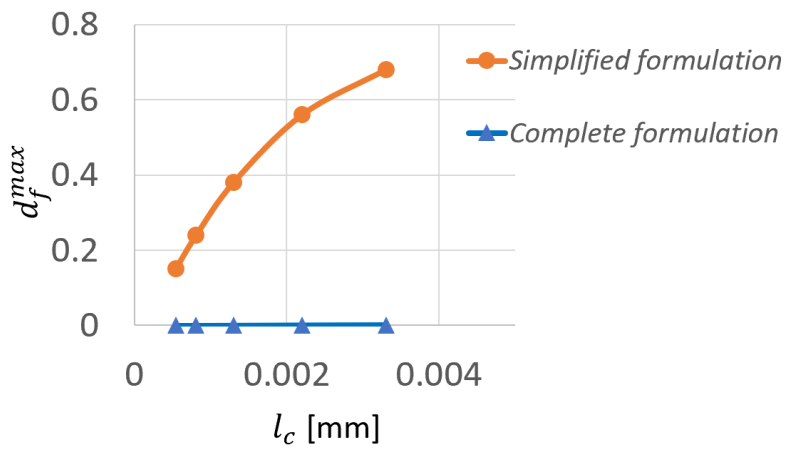

Figure 7: The maximum damage d_f^{max} in the fiber at the final failure state for different l_c values and for the two half fibers model by applying different formulations.

values. From $l_c = 1.30 \times 10^{-3}$ mm, a necking effect on the diffusive crack band can be observed because the diffusive crack bandwidth is larger than the l_f values, and the fiber is much more difficult to be damaged.

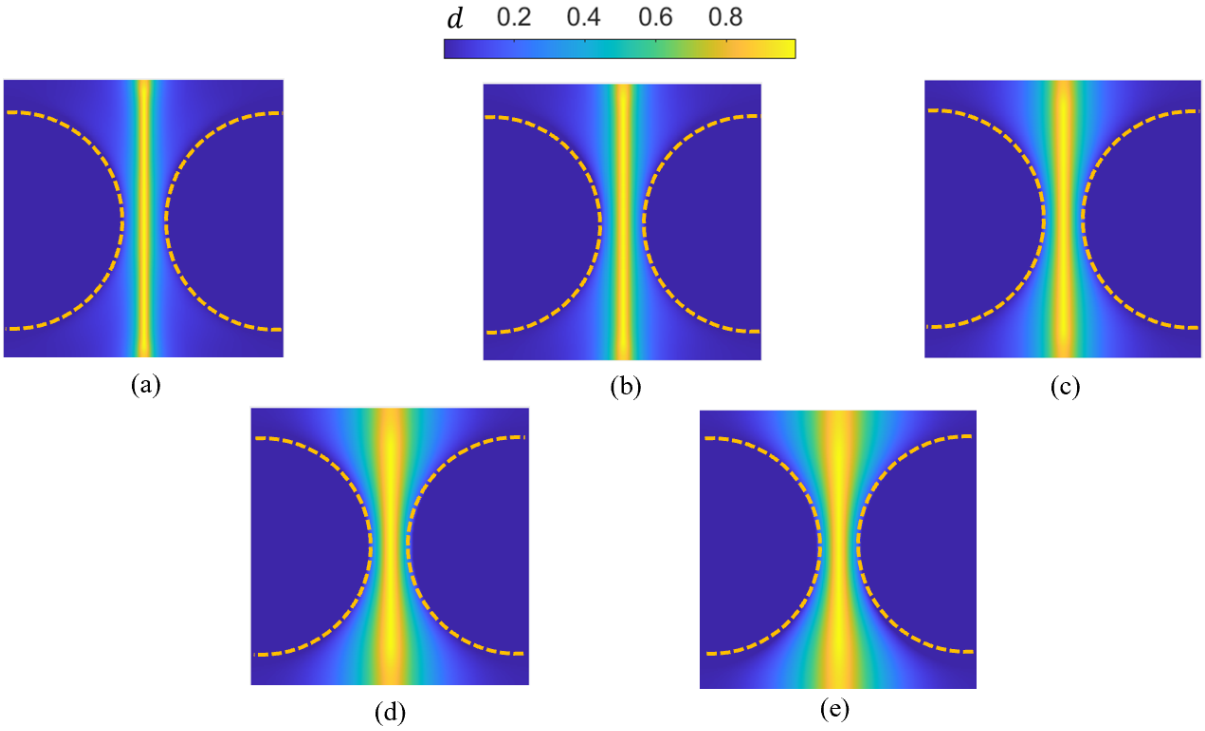

Figure 8: The local damage fields at the final failure state for different l_c values and for the two half fibers model by applying the complete formulation: (a) 5.40×10^{-4} mm; (b) 8.10×10^{-4} mm; (c) 1.30×10^{-3} mm; (d) 2.20×10^{-3} mm; (e) 3.30×10^{-3} mm. The orange dashed lines are the fiber contours.

The damage profiles along the center line for the complete formulation are plotted in Fig. 9. This figure confirms that the damage in fibers would decrease to almost zero no matter the l_c values.

The differences between the simplified and complete formulations on macro-level stress-strain relations are shown in Fig. 10. This figure shows that the complete formulation shows higher peak stress and final failure strain than the simplified formulation. The effect of the damage diffusion on the macroscopic stress-strain curves is not obvious for a smaller l_c value (5.40×10^{-4} mm), while it becomes more and more significant as l_c increases. However, a conclusion can be obtained: for heterogeneous models, especially

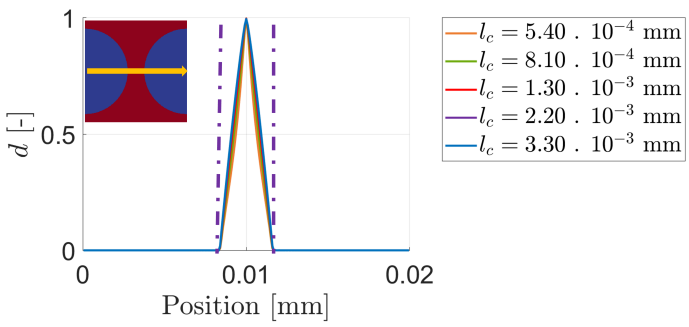

Figure 9: The damage profiles along the center line for different l_c values and for the two half fibers model by applying the complete formulation. The purple dashed lines are boundaries between fibers and matrix.

when a large l_c is being used, the additional term in the complete formulation has a significant influence on both local crack patterns and macro-level mechanical behaviors.

4.1.3 Study of iteration numbers for convergence

The above results show that the complete formulation eliminates unphysical damage diffusion between phases. However, adding the additional term (shown in Eq. (14)) gives a high cost. Fig. 11 provides the total fixed-point iterations of the simplified and complete formulations. As can be seen, the complete formulation needs much larger iteration numbers to get convergence than the simplified formulation. This difference is more than 10^2 times.

4.2 Single notch model

To better understand the impact of Anderson's acceleration scheme and the contrast of damage properties, a simpler model (single-notch model) is studied in this work. As shown in Fig. 12, it is a square plate of a length of 1 mm. A straight horizontal notch of 5.00×10^{-1} mm is located at the mid-height of the left edge. The width of the notch is one voxel size. Because the FFT-based solver is intrinsically periodic, we need to add lateral bands, denoted as M2 (purple material), to break the periodicity and mimic the stress-free boundary conditions. Material M2 is also used for the notch. Note that, in this study, the resolution is given as $N = 251$ (mesh size $h = 4.00 \times 10^{-3}$ mm) and

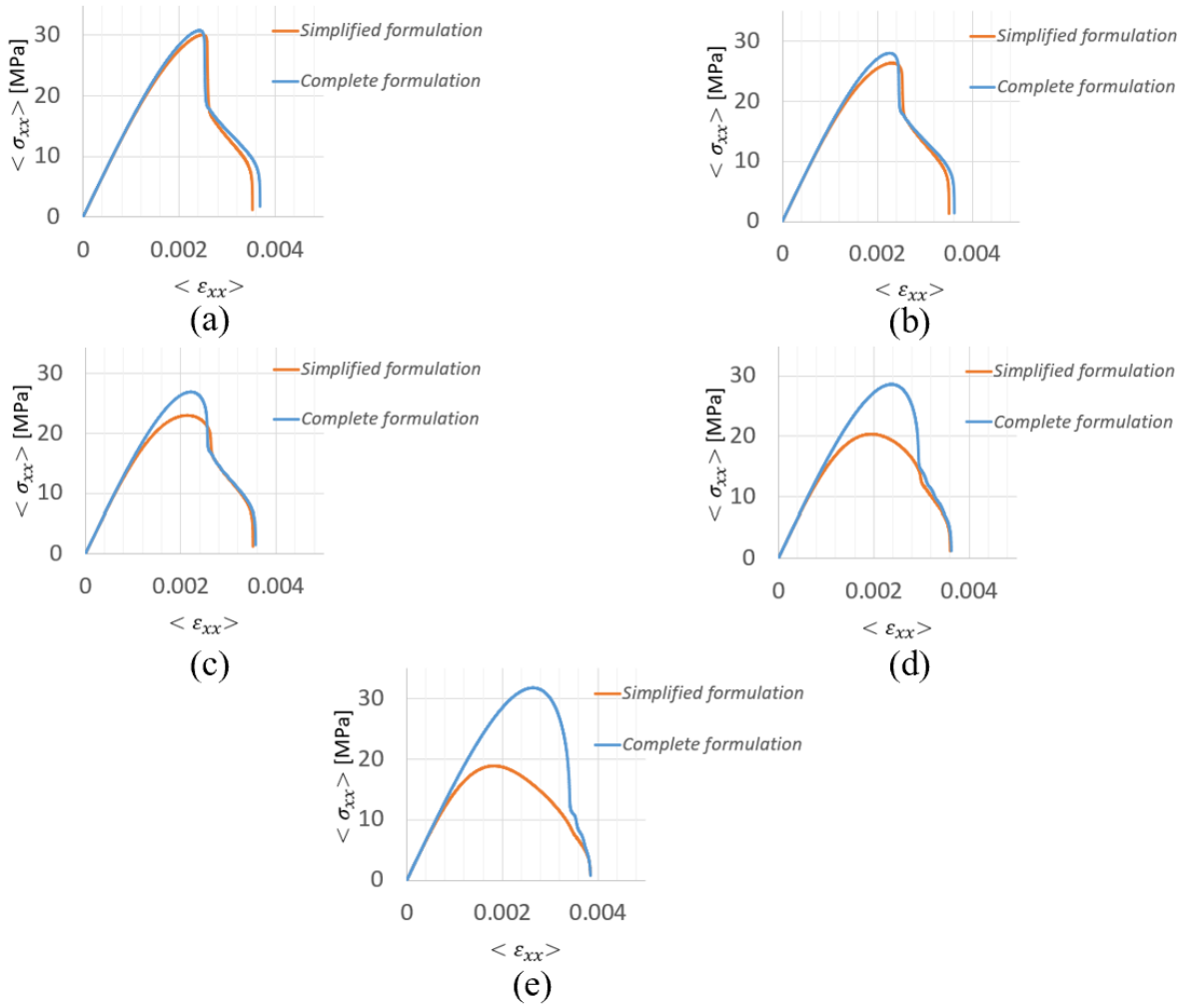

Figure 10: The macro-level $\sigma - \varepsilon$ relations for different l_c values and for the two half fibers model by applying different formulations: (a) 5.40×10^{-4} mm; (b) 8.10×10^{-4} mm; (c) 1.30×10^{-3} mm; (d) 2.20×10^{-3} mm; (e) 3.30×10^{-3} mm.

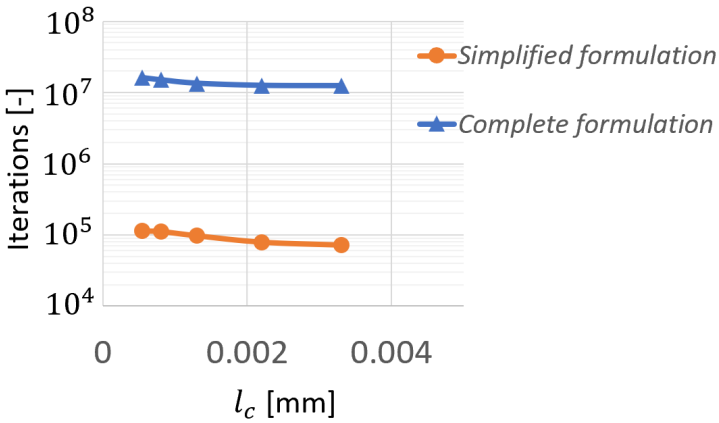

Figure 11: Total fixed-point iteration numbers from the beginning of the loading to the final failure state for the two half fibers model.

$l_c = 2 \times 10^{-2}$ mm.

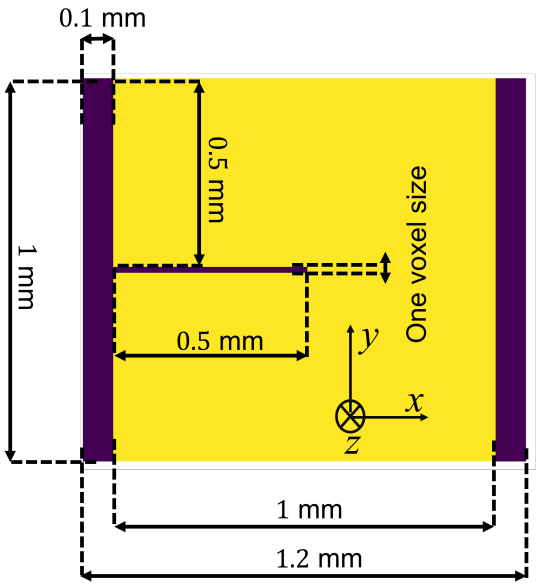

Figure 12: The geometry of the single notch plate. Material 1 (M1) and material 2 (M2) are the yellow and purple parts, respectively.

In this study, the following material parameters are adopted for M1: Young's modulus of $E = 2.10 \times 10^2$ GPa, Poisson's ratio of $\nu = 0.3$, and critical energy release rate of $G_c = 2.70\,\mathrm{N\,mm^{-1}}$. Besides, the void-like properties of M2 are: $E^e = 2.10 \times 10^{-2}$ GPa, $\nu^e = 0.3$. As for G_c^e, three values are chosen (Table 2).

For all three tests, a tensile loading along $y-$direction with time step $\delta\langle\varepsilon_{yy}\rangle = 5.00 \times 10^{-7}$

	Test 1	Test 2	Test 3
G_c^e (N mm^{-1})	2.70	27	2700
Contrast G_c^e/G_c	1	10	1000

Table 2: The damage properties for the three tests on the single notch model.

is applied while stress-free conditions are imposed in other directions ($\langle\sigma_{xx}\rangle = \langle\sigma_{zz}\rangle = \langle\sigma_{xy}\rangle = \langle\sigma_{xz}\rangle = \langle\sigma_{yz}\rangle = 0$). The solutions computed for all values of G_c and for the two formulations were the same and correspond to the result in Ref. [24], with the crack propagating along the same line as the pre-crack. The local damage fields are not reported herein as we are only interested in the influence of the contrast on the iteration numbers.

Fig. 13 shows the total fixed-point iteration numbers with different contrasts. Compared to the simplified formulation, the complete formulation is sensitive to the contrast of damage properties. The higher the contrast is, the more iterations are required. Moreover, the slope of the complete formulation is almost linear. Furthermore, Fig. 13 also indicates that Anderson's acceleration scheme can significantly reduce the iteration numbers. However, for the complete formulation, it is much less effective for a high contrast model. Hence, a more efficient acceleration algorithm needs to be proposed in the future when dealing with high contrast mediums.

4.3 Single fiber unit-cell with notch defect under tension

In this third example, a single fiber unit-cell model with a notch defect is studied.

As shown in Fig. 14, a notch of 6.00×10^{-3} mm is placed at the mid-height of the left edge with one voxel width. The model is a square plate of 2.00×10^{-2} mm with a thickness of one voxel in the third direction. The circular reinforced fiber is at the mid-height with a diameter of 6.00×10^{-3} mm and 1.30×10^{-2} mm away from the left edge. Because the FFT solver is intrinsically periodic, we need to add lateral bands. Each lateral band has a width of five voxels. Meanwhile, the material of the lateral bands is also used for

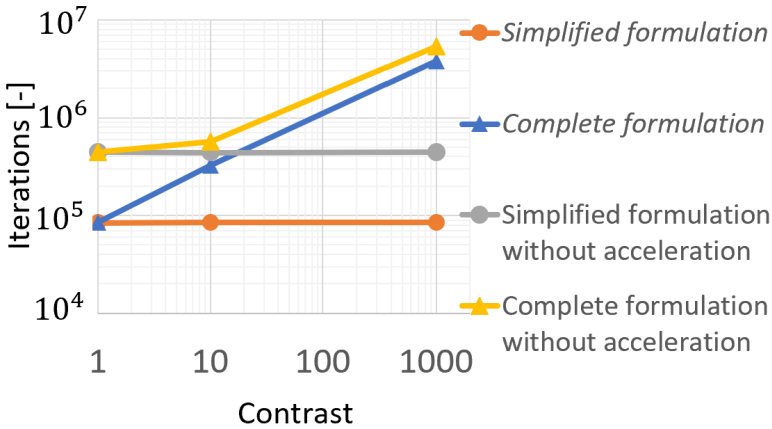

Figure 13: Total numbers of fixed-point iterations for the phase-field solution from the beginning of the loading to the final failure state for the single notch model.

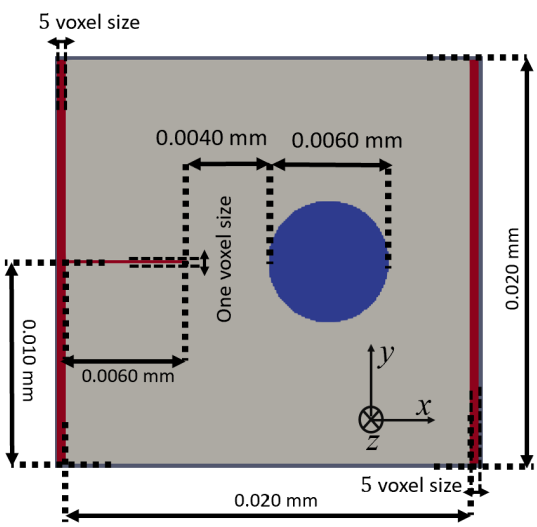

Figure 14: The geometry of composite model with defect (blue: fiber; grey: matrix; red: notch).

the notch. The resolution is $N = 225$, the same as in Sec. 4.1, and gives a voxel size $h = 8.89 \times 10^{-5}\,\mathrm{mm}$.

Regarding the material properties, the fiber (blue part) is E-glass with properties: $E_f = 7.40 \times 10^1\,\mathrm{GPa}$, $\nu_f = 0.2$, and $G_c^f = 6.00 \times 10^1\,\mathrm{N\,mm^{-1}}$. These values are chosen to prevent failure of the fibers. The gray region is the matrix for which the material is Epoxy with properties: $E_m = 4.65\,\mathrm{GPa}$, $\nu_m = 0.35$, $G_c^m = 9.60 \times 10^{-4}\,\mathrm{N\,mm^{-1}}$. These two materials are the same as in Sec. 4.1. For the lateral bands and notch, where there should be a void, one ten-thousandth of matrix elastic properties are taken to avoid the convergence issue. They are: $E_0^e = 4.65 \times 10^{-4}\,\mathrm{GPa}$, $\nu^e = 0.35$, and $G_c^e = 9.60 \times 10^{-4}\,\mathrm{N\,mm^{-1}}$, the same as the matrix.

The l_c values are taken from $l_c = 2.70 \times 10^{-4}\,\mathrm{mm}$, which satisfies Miehe's criterion $l_c^{min}/h \approx 3.00 > 2.00$. For all tests, a tensile loading along $y-$direction with time step $\delta\langle\varepsilon_{yy}\rangle = 5.00 \times 10^{-7}$ is applied while stress-free conditions are imposed in other directions ($\langle\sigma_{xx}\rangle = \langle\sigma_{zz}\rangle = \langle\sigma_{xy}\rangle = \langle\sigma_{xz}\rangle = \langle\sigma_{yz}\rangle = 0$).

The results of local fields for different l_c values are shown in Fig. 15. As seen in the figure, both formulations can capture the complex crack propagation pattern. A similar phenomenon in Sec. 4.1 can also be observed herein: the frontiers between fiber and matrix can be observed in the complete formulation, while this transition is smeared out in the simplified formulation. The larger the l_c is, the more critical the damage diffusion is. This phenomenon can be shown in profile plots as shown in Fig. 16. In contrast, the complete formulation does not have this issue. In this part of the work, our scope is to analyze the damage state in the matrix and fiber. Thus, the damage in the notch is not our focus point and is not plotted in Fig. 16.

We also observe in Fig. 15(c,f) the diffusion of damage within each phase, as there are non-zero damage values away from the crack in the matrix phase. This is a well-known property of Miehe's phase-field model that has been eliminated in alternative models [9]. Its analysis is out of the scope of the present work as it is a modeling issue that is not specific to the FFT-based method and heterogeneous materials.

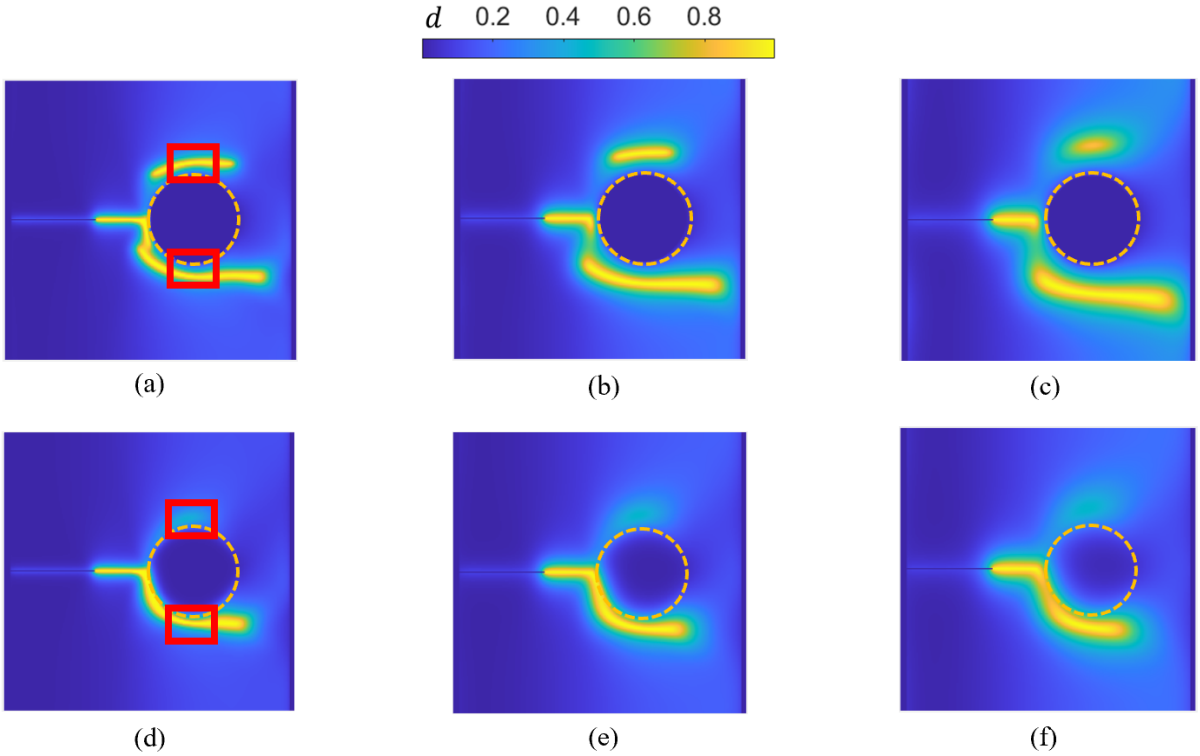

Figure 15: The local damage fields for different l_c values and for the model with notch and fiber under tension by applying the complete (top) and simplified formulations (bottom): (a,d) $l_c = 2.70 \times 10^{-4}$ mm; (b,e) $l_c = 5.40 \times 10^{-4}$ mm; (c,f) $l_c = 8.10 \times 10^{-4}$ mm. The orange dashed lines are the fiber contours, and the red zone is explained in the text.

Crack propagation patterns predicted using the complete formulation (Fig. 15(a,b,c)) seem challenging to explain from a physical standpoint. After studying the whole damage process, we observe that the two formulations actually share the same first stage. For instance in the simulations with $l_c = 2.70 \times 10^{-4}$ mm, the crack initiates from the notch and propagates until the fiber where it is arrested in the first stage. Then, in the second stage, which is also similar for both formulations, the damage in the matrix continues increasing in the red zones shown in Fig. 15(a,d) rather than at the crack initiated in the first stage. Finally, one or two new cracks initiate in these red zones and propagate until joining the initial crack. Animated pictures showing the second and third stages can be found in the supplementary material.

The difference between the two formulations is that the complete formulation shows later failure, which makes the initiation of cracks in both red zones possible. It is possible that this phenomenon that may seem unphysical is due to the absence of a debonding model at the interface. In this work, indeed, the fracture properties of the interface are simply that of the matrix. This issue might be dealt with by introducing a debonding model in the complete formulation. This will be considered in future work.

Fig. 17 shows the macro-level $\sigma - \varepsilon$ relations with different formulations. This figure re-emphasizes that the term $\nabla (G_c l_c) \cdot \nabla d$ produced non-negligible effects in the high contrast heterogeneous models. The complete formulation offers a higher final failure strain than the simplified formulation. However, the two formulations have similar responses for the low-level damage state, which can also be observed in Sec. 4.1. That is mainly because the ∇d value is small for the low-level damage state, which reduces the effect of the term $\nabla (G_c l_c) \cdot \nabla d$.

The tests above (Fig. 15) have shown that the complete formulation can avoid the unrealistic fiber damage for a high contrast model ($G_c^f \gg G_c^m$). We conduct another series of tests to verify whether the complete formulation can break two phases for low contrast ($G_c^f \approx G_c^m$). Hence, in these tests, the matrix properties are unchanged while the fiber properties are reduced to twice those of the matrix ($E_f = 2E_m$ and $G_f = 2G_m$).

Fig. 18 shows that the complete formulation can break two phases as the simplified formulation does. The results of the two formulations are also similar from the point of

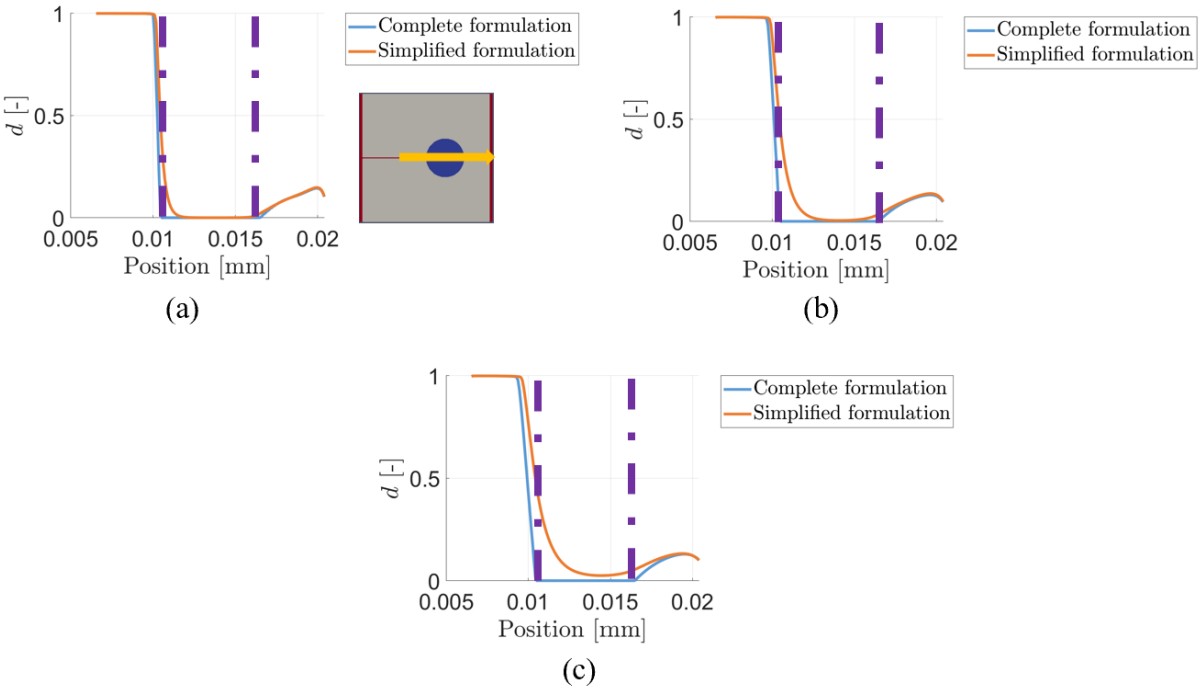

Figure 16: The damage profiles along the center-line for various l_c values and for the model with notch and fiber under tension by applying the complete and simplified formulations: (a) $l_c = 2.70 \times 10^{-4}$ mm; (b) $l_c = 5.40 \times 10^{-4}$ mm; (c) $l_c = 8.10 \times 10^{-4}$ mm. The purple dashed lines are boundaries between fibers and matrix.

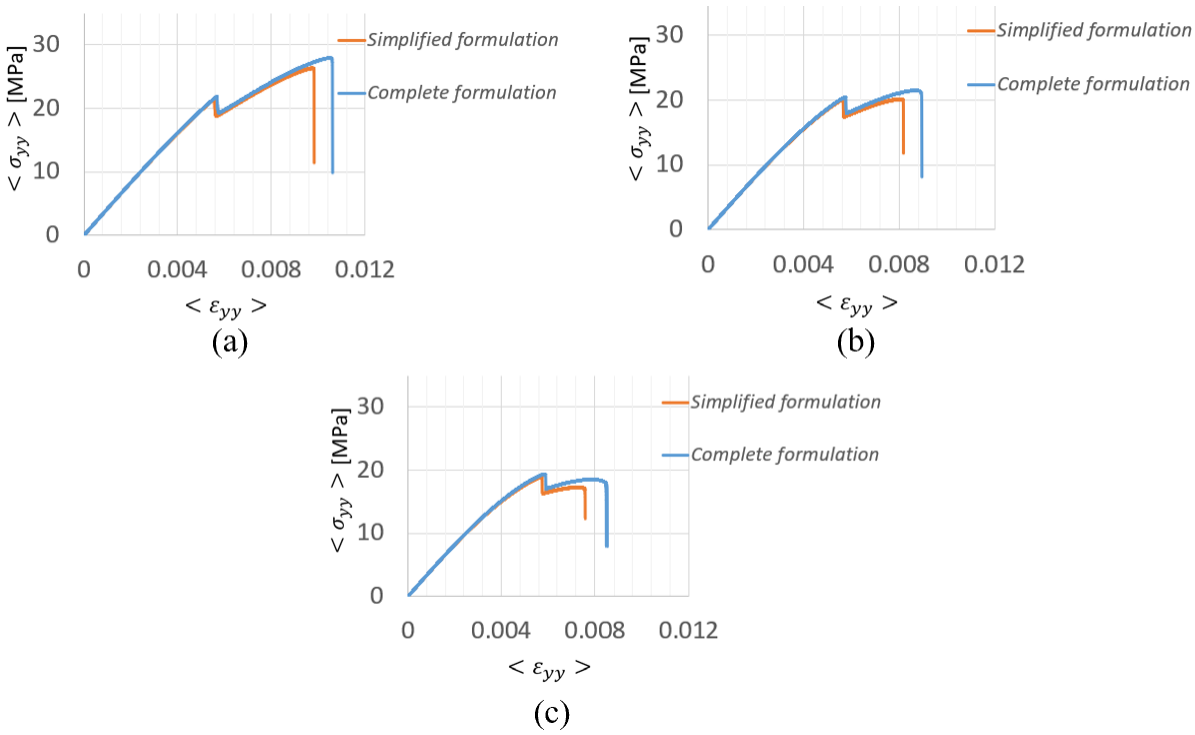

Figure 17: The macro-level $\sigma - \varepsilon$ relations for different l_c values and for the model with notch and fiber under tension: (a) $l_c = 2.70 \times 10^{-4}$ mm; (b) $l_c = 5.40 \times 10^{-4}$ mm; (c) $l_c = 8.10 \times 10^{-4}$ mm.

view of local damage fields. Meanwhile, according to Fig. 19, the difference in macro-level $\sigma - \varepsilon$ relations between the two formulations is reduced for a low contrast model. In conclusion, the lower the contrast is, the more similar the results are.

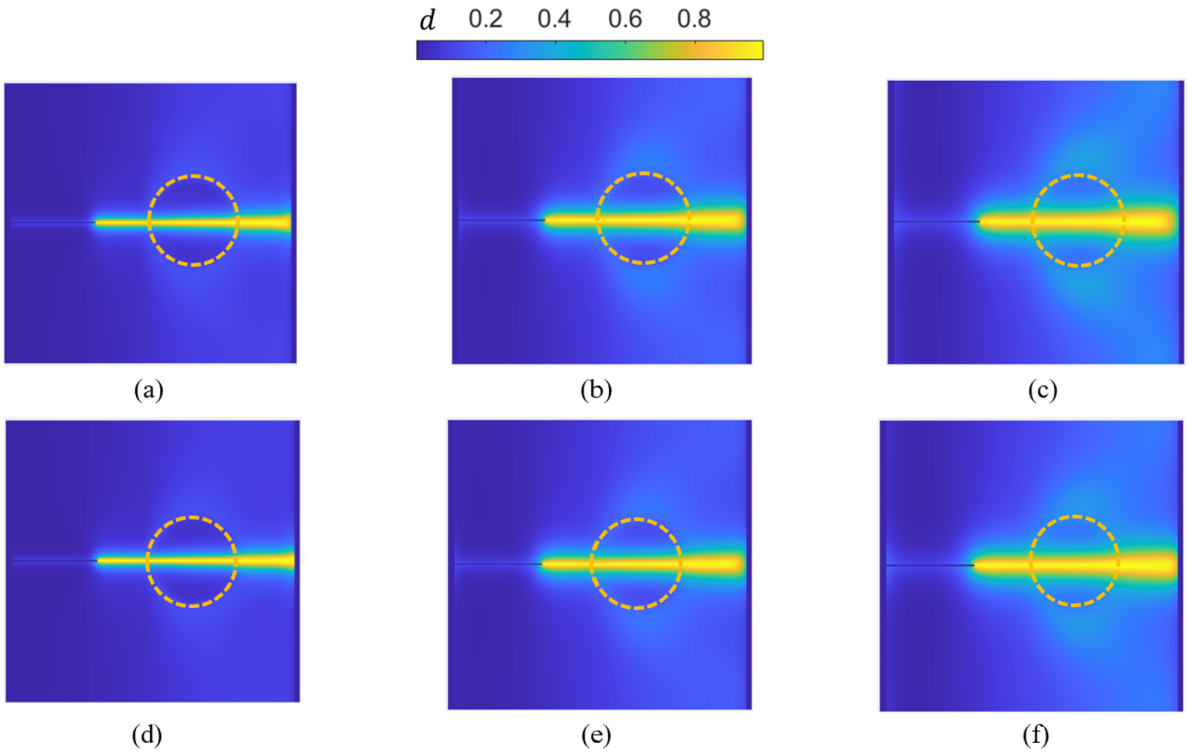

Figure 18: The local damage fields for different l_c values and for the model with notch and fiber under tension by applying the complete (top) and simplified formulations (bottom): (a,d) $l_c = 2.70 \times 10^{-4}$ mm; (b,e) $l_c = 5.40 \times 10^{-4}$ mm; (c,f) $l_c = 8.10 \times 10^{-4}$ mm. The orange dashed lines are the fiber contours.

4.4 Single fiber unit-cell with notch defect under shear

To compare the two formulations under different loading conditions, we simulate a model similar to that used in Sec. 4.3 under in-plane shear loading. We delete the two lateral bands, which results in the periodic model shown in Fig. 20.

The materials and properties are the same as in Sec. 4.3. The loading conditions are similar, except that the strain is imposed in direction xy in this section, and the stresses

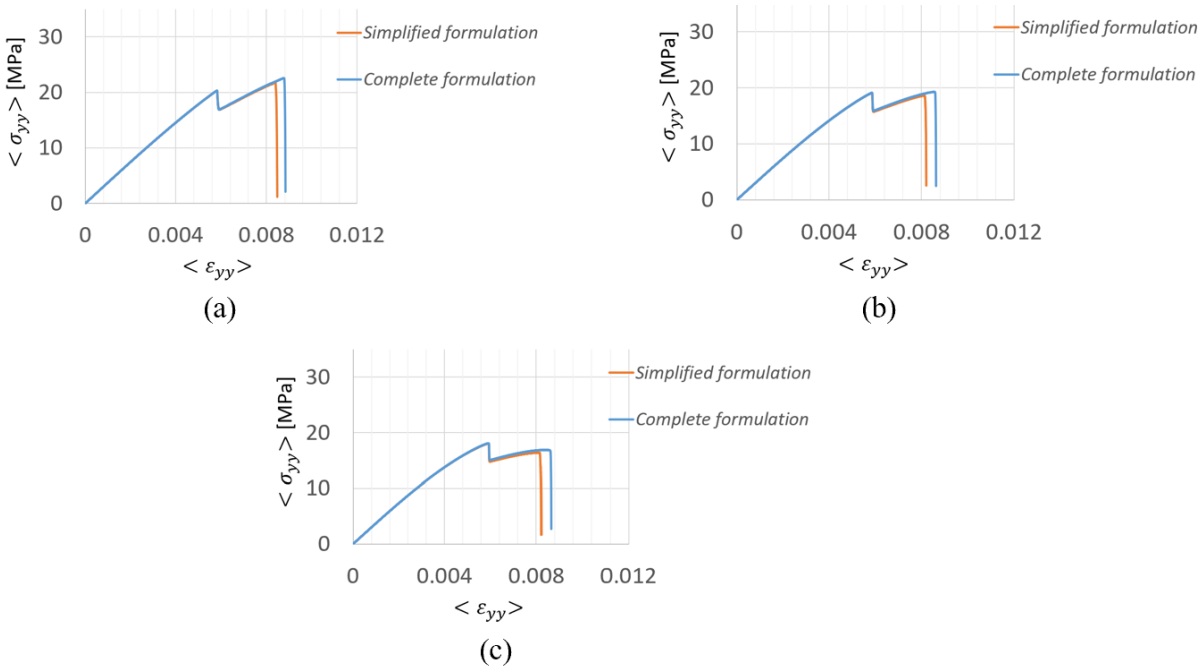

Figure 19: The macro-level $\sigma - \varepsilon$ relations for different l_c values and for the model with notch and fiber under tension: (a) $l_c = 2.70 \times 10^{-4}$ mm; (b) $l_c = 5.40 \times 10^{-4}$ mm; (c) $l_c = 8.10 \times 10^{-4}$ mm.

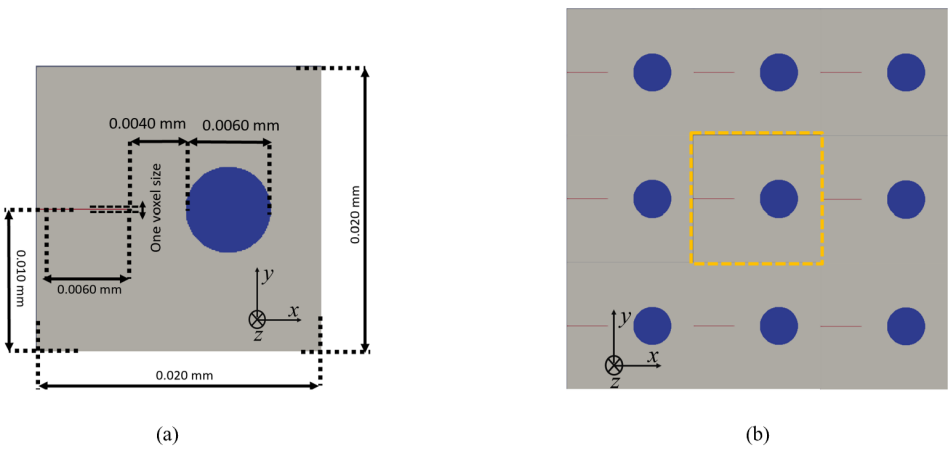

Figure 20: (a) The geometry for the single fiber unit-cell with periodic notch defect test case. (b) Infinite periodic medium from which this unit-cell is extracted (orange square).

in the other directions are free.

The results are shown in Fig. 21. Both the simplified and complete formulations predict well the in-plane shear crack patterns. Note that the cracks in the red zones are mainly due to the periodic boundary conditions. In these results, because the cracked zones are far from the interface between the fiber and the matrix, it can be seen that the predictions of these two formulations show less difference in terms of local-level crack patterns and macro-level mechanical responses. We can conclude that the difference between the two formulations should be less pronounced when the crack initiates and propagates away from the interfaces.

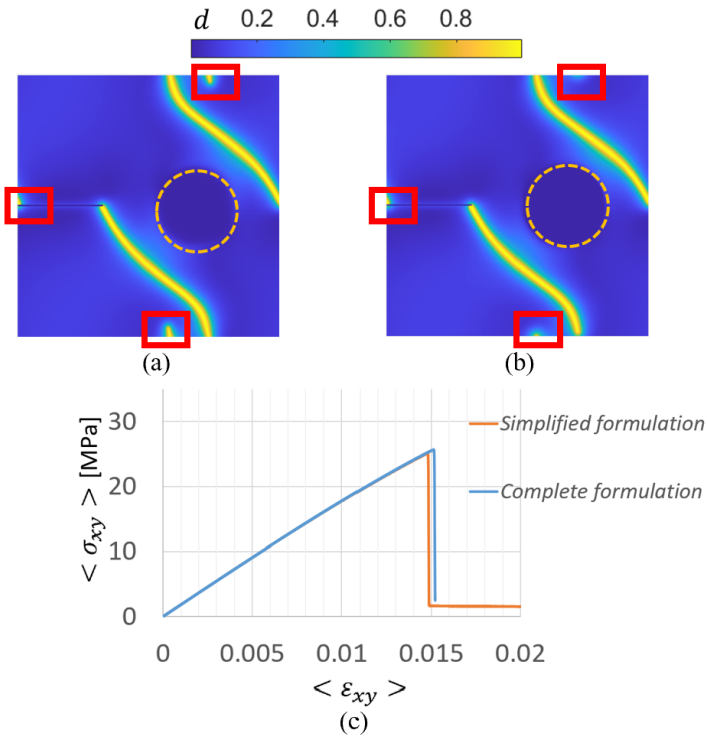

Figure 21: The local damage fields at final failure for $l_c = 2.70 \times 10^{-4}$ mm and for the model with notch and fiber under shear: (a) the simplified formulation, (b) the complete formulation. (c) The macro-level $\sigma - \varepsilon$ relations. The orange dashed lines are the fiber contours.

4.5 Multi-fiber model

According to the above tests, we have shown that the simplified formulation can lead to a non-physical damage diffusion for a multi-phase heterogeneous model, *e.g.*, composites, while the complete formulation avoids this. The above tests only show simple examples. Thus, a more complex model corresponding to a unidirectional fiber-reinforced composite material is tested in this part. This model shown in Fig. 22 is reproduced from Ref. [14] as well as the material properties: the blue part is fiber, of which the material is E-glass with properties: $E_f = 7.40 \times 10^1$ GPa and $\nu_f = 0.20$. The value of G_C^f is not given in Ref. [14] hence we assume that $G_c^f = 6.00 \times 10^1\,\mathrm{N\,mm^{-1}}$ based on Ref. [24]. The red part is the matrix, of which the material is Epoxy with properties: $E_m = 4.65\,\mathrm{GPa}$, $\nu_m = 0.35$, $G_c^m = 9.60 \times 10^{-4}\,\mathrm{N\,mm^{-1}}$.

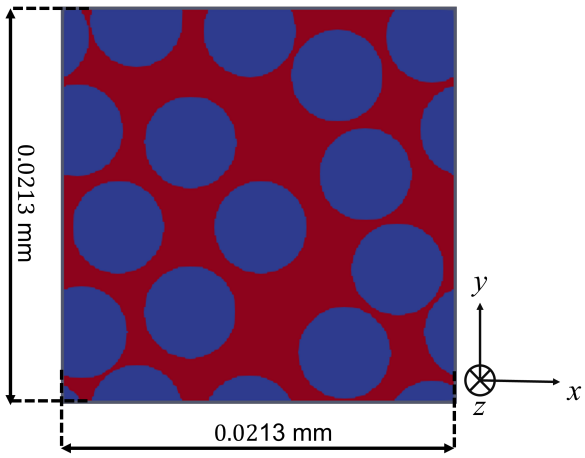

Figure 22: The complex model with multiple fibers inspired from Ref. [14].

The model size is 2.13×10^{-2} mm with a resolution of $N = 225$, and only one voxel is used in the thickness. Note that the fiber volume fraction is $V_f = 0.60$, and $l_c = 2.90 \times 10^{-4}$ mm ensures that $l_c/h > 2$. The model is subjected to a macroscopic strain along the x- direction (transverse direction) with a time step $\delta\langle\varepsilon_{xx}\rangle = 5.00 \times 10^{-7}$ until the final failure while stress-free conditions are imposed in the other directions ($\langle\sigma_{yy}\rangle = \langle\sigma_{zz}\rangle = \langle\sigma_{xy}\rangle = \langle\sigma_{xz}\rangle = \langle\sigma_{yz}\rangle = 0$).

The result for the simplified formulation is shown in Fig. 23(a,b). We observe once again a diffusion of damage from the matrix to the fibers. This re-confirms the damage diffusion

between phases for the simplified formulation. As demonstrated previously for a simple model, the result obtained using an unrealistically large value for G_c^f in Fig. 23(c,d) shows that the micro-level damage fields, especially the fiber damage, do not vary. Fig. 23(e) demonstrates that the macro-level mechanical response does not vary either when increasing G_c^f to unrealistically large values.

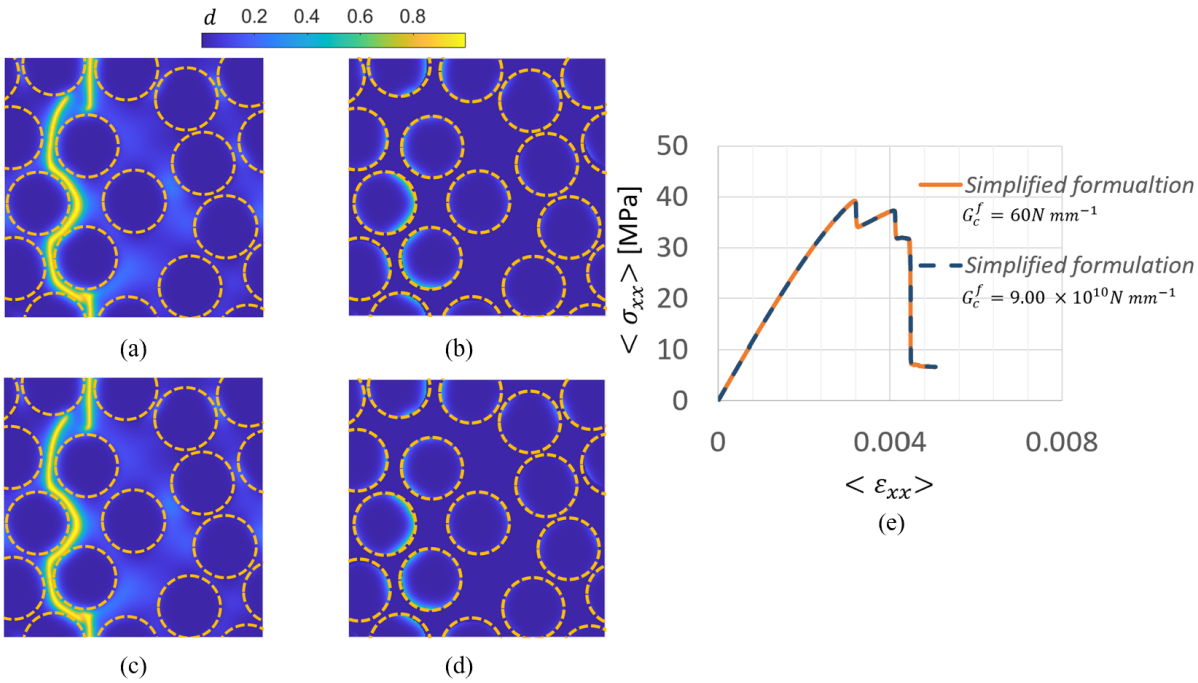

Figure 23: The local damage fields at final failure for the complex model using the simplified formulation with $l_c = 2.90 \times 10^{-4}$ mm: (a) $G_c^f = 6.00 \times 10^1\,\mathrm{N\,mm^{-1}}$, (c) $G_c^f = 9.00 \times 10^{10}\,\mathrm{N\,mm^{-1}}$. The fiber damage fields at the same state: (b) $G_c^f = 6.00 \times 10^1\,\mathrm{N\,mm^{-1}}$, (d) $G_c^f = 9.00 \times 10^{10}\,\mathrm{N\,mm^{-1}}$. (e) The macro-level $\sigma - \varepsilon$ relations. The orange dashed lines are the fiber contours.

The comparison between the two formulations is shown in Fig. 24. It clearly shows that the complete and simplified formulations can give totally different results for micro-level damage fields and macro-level mechanical responses as well. This is because the l_c value is large compared to the inter-fiber distance l_f in the model. This is challenging because we can neither reduce l_c due to Miehe's criterion ($l_c/h > 2$) and its implication on computational cost nor arbitrarily increase l_f because it depends on the material. Meanwhile, it should be admitted that we cannot judge which results are correct without

experimental results. Unfortunately, Ref. [14] also lacks experimental results and uses another type of phase-field that is not comparable. Thus, more studies should be carried out in the future to validate the complete formulation's reliability.

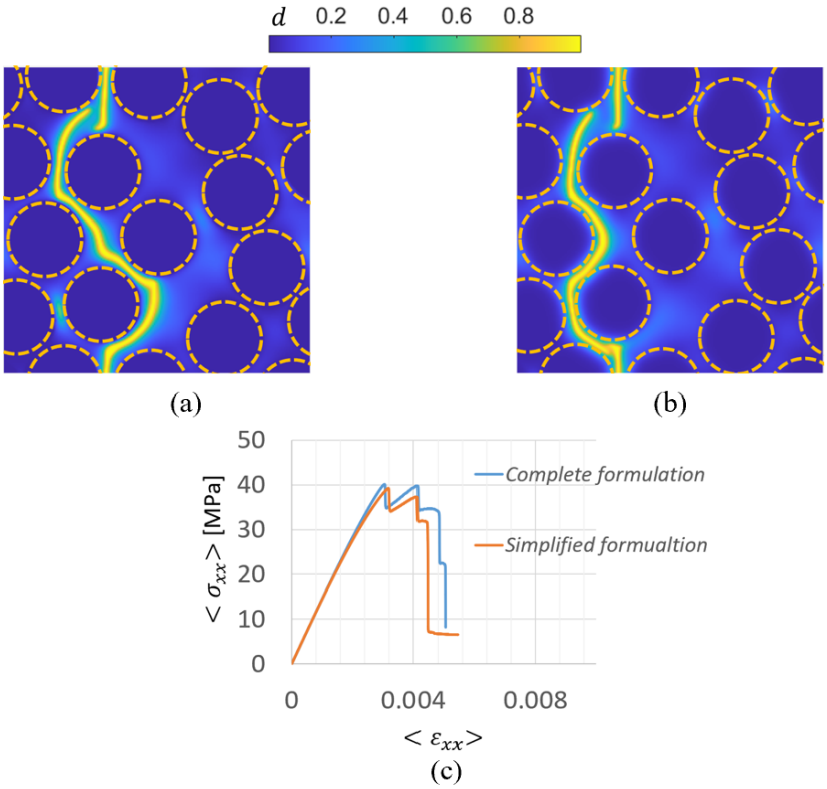

Figure 24: The local damage fields at final failure for the complex model with $l_c = 2.90 \times 10^{-4}$ mm: (a) the complete formulation, (b) the simplified formulation. (c) The macro-level $\sigma - \varepsilon$ relations. The orange dashed lines are the fiber contours.

This multi-fiber model can be a basis for a thorough validation of the model in a future work. Micro-configuration of the fiber debonding cracks can be observed in-situ, as done for example in Refs. [32, 33]. The important features of this phenomenon are an angle between the debonded surface of fibres and the sequence of linking of the debonding cracks into a continuous transverse crack. The ability of a model to represent such features for a microstructural configuration of fibres taken from in-situ micrographs should be a validation criterion.

5 Conclusions

In this paper, two formulations of a phase-field model are addressed and compared: one is called the simplified formulation, while another is called the complete formulation. The main difference between these two formulations is that the term $\nabla(G_c l_c) \cdot \nabla d$ is omitted in the simplified formulation, where details can be found in Eq. (14). For a homogeneous model, these two formulations are equivalent. In contrast, for a heterogeneous model, the results of the two formulations diverge because the G_c values are not constant anymore. The higher the contrast is, the more critical the divergence is.

The simplified formulation can converge much faster than the complete formulation. For the same problem, the complete formulation requires more iteration numbers for convergence. The higher the contrast is, the more obvious the difference is. One critical aspect, however, can be observed when using the simplified formulation for a heterogeneous model: non-physical damage diffusion occurs between phases. This diffusion is eliminated with the complete formulation. It highly impacts the evaluation of the local micro-level damage state. The difference in macro-level $\sigma - \varepsilon$ relations between the two formulations cannot be neglected either. The larger the l_c value is and the closer to the interfaces the cracks are, the more obvious these two phenomena are.

Moreover, for Miehe's phase-field model, the l_c value plays a vital role in the mechanical response, which is often considered a material parameter in the literature. This parameter cannot, therefore, be arbitrarily reduced in order to diminish the difference between the simplified and complete formulations. Quantitative comparisons with experimental tests should hence be carried out in future work to find out which formulation is more reliable.

In the present work, Anderson's acceleration algorithm has been applied to speed up the convergence. Despite this, when applying the complete formulation, Fig. 13 shows that the increase in iteration numbers compared to the simplified formulation cannot be neglected. Besides, Anderson's acceleration scheme becomes less efficient for large contrast models. Thus, proposing a sufficiently efficient acceleration algorithm is one of the important perspectives for the next step. Replacing the basic-scheme and its truncated Green operator by more robust alternatives might also alleviate the influence

of the contrast on the iteration numbers.

Meanwhile, the authors also noticed that a multi-phase-field technique for heterogeneous mediums has been proposed to solve the above issues. One of the main drawbacks of the multi-phase-field approach is to create one phase-field for each phase. That will increase the complexity when dealing with models with a large number of phases. In contrast, the complete formulation only needs one formulation to describe all phases. Thus, it will also be interesting to compare the efficiency of these two approaches in the future.

References

[1] A. Griffith, "Vi. the phenomena of rupture and flow in solids," *Philosophical Transactions of the Royal Society of London. Series A, Containing Papers of a Mathematical or Physical Character*, vol. 221, pp. 163–198, 1921.

[2] G. R. Irwin, "Analysis of stresses and strains near the end of a crack traversing a plate," *Journal of Applied Mechanics*, vol. 24, no. 3, pp. 361–364, 1957.

[3] B. Bourdin, G. Francfort, and J.-J. Marigo, "Numerical experiments in revisited brittle fracture," *Journal of the Mechanics and Physics of Solids*, vol. 48, no. 4, pp. 797–826, 2000.

[4] B. Bourdin, G. A. Francfort, and J.-J. Marigo, "The variational approach to fracture," *Journal of Elasticity*, vol. 91, pp. 5–148, 2008.

[5] G. Francfort and J.-J. Marigo, "Revisiting brittle fracture as an energy minimization problem," *Journal of the Mechanics and Physics of Solids*, vol. 46, no. 8, pp. 1319–1342, 1998.

[6] R. de Borst and C. V. Verhoosel, "Gradient damage vs phase-field approaches for fracture: Similarities and differences," *Computer Methods in Applied Mechanics and Engineering*, vol. 312, pp. 78–94, 2016.

[7] T. K. Mandal, V. P. Nguyen, and A. Heidarpour, "Phase field and gradient enhanced damage models for quasi-brittle failure: A numerical comparative study," *Engineering Fracture Mechanics*, vol. 207, pp. 48–67, 2019.

[8] K. Pham, H. Amor, J.-J. Marigo, and C. Maurini, "Gradient damage models and their use to approximate brittle fracture," *International Journal of Damage Mechanics*, vol. 20, no. 4, pp. 618–652, 2011.

[9] J.-Y. Wu, V. P. Nguyen, C. T. Nguyen, D. Sutula, S. Sinaie, and S. P. Bordas, "Phase-field modeling of fracture," in *Advances in Applied Mechanics* (S. P. Bordas and D. S. Balint, eds.), vol. 53, pp. 1–183, Elsevier, 2020.

[10] C. Miehe, F. Welschinger, and M. Hofacker, "Thermodynamically consistent phase-field models of fracture: Variational principles and multi-field fe implementations," *International Journal for Numerical Methods in Engineering*, vol. 83, no. 10, pp. 1273–1311, 2010.

[11] C. Miehe, M. Hofacker, and F. Welschinger, "A phase field model for rate-independent crack propagation: Robust algorithmic implementation based on operator splits," *Computer Methods in Applied Mechanics and Engineering*, vol. 199, no. 45, pp. 2765–2778, 2010.

[12] M. Ambati, T. Gerasimov, and L. De Lorenzis, "A review on phase-field models of brittle fracture and a new fast hybrid formulation," *Computational Mechanics*, vol. 55, pp. 383–405, 2015.

[13] T. Nguyen, J. Yvonnet, Q.-Z. Zhu, M. Bornert, and C. Chateau, "A phase field method to simulate crack nucleation and propagation in strongly heterogeneous materials from direct imaging of their microstructure," *Engineering Fracture Mechanics*, vol. 139, pp. 18–39, 2015.

[14] J. Espadas-Escalante, N. van Dijk, and P. Isaksson, "A phase-field model for strength and fracture analyses of fiber-reinforced composites," *Composites Science and Technology*, vol. 174, pp. 58–67, 2019.

[15] P. Zhang, X. Hu, S. Yang, and W. Yao, "Modelling progressive failure in multi-phase materials using a phase field method," *Engineering Fracture Mechanics*, vol. 209, pp. 105–124, 2019.

[16] Y. Chen, L. Gélébart, A. Marano, and J. Marrow, "Fft phase-field model combined with cohesive composite voxels for fracture of composite materials with interfaces," *Computational Mechanics*, vol. 68, pp. 433–457, 2021.

[17] T. Nguyen, J. Yvonnet, M. Bornert, C. Chateau, F. Bilteryst, and E. Steib, "Large-scale simulations of quasi-brittle microcracking in realistic highly heterogeneous microstructures obtained from micro ct imaging," *Extreme Mechanics Letters*, vol. 17, pp. 50–55, 2017.

[18] H. Moulinec and P. Suquet, "A fast numerical method for computing the linear and nonlinear mechanical properties of composites," *Comptes rendus de l'Académie des sciences. Série II, Mécanique, physique, chimie, astronomie*, vol. 318, no. 11, pp. 1417–1423, 1994.

[19] H. Moulinec and P. Suquet, "A FFT-Based Numerical Method for Computing the Mechanical Properties of Composites from Images of their Microstructures," in *IUTAM Symposium on Microstructure-Property Interactions in Composite Materials*, pp. 235–246, Springer Netherlands, 1995.

[20] H. Moulinec and P. Suquet, "A numerical method for computing the overall response of nonlinear composites with complex microstructure," *Computer Methods in Applied Mechanics and Engineering*, vol. 157, no. 1-2, pp. 69–94, 1998.

[21] Y. Chen, L. Gélébart, C. Chateau, M. Bornert, C. Sauder, and A. King, "Analysis of the damage initiation in a SiC/SiC composite tube from a direct comparison between large-scale numerical simulation and synchrotron X-ray micro-computed tomography," *International Journal of Solids and Structures*, vol. 161, pp. 111–126, 2019.

[22] "FFTW." http://www.fftw.org.

[23] X. Ma, M. Shakoor, D. Vasiukov, S. V. Lomov, and C. H. Park, "Numerical artifacts of fast fourier transform solvers for elastic problems of multi-phase materials: their causes and reduction methods," *Computational Mechanics*, vol. 67, pp. 1661–1683, 2021.

[24] Y. Chen, D. Vasiukov, L. Gélébart, and C. H. Park, "A fft solver for variational phase-field modeling of brittle fracture," *Computer Methods in Applied Mechanics and Engineering*, vol. 349, pp. 167–190, 2019.

[25] F. Ernesti, M. Schneider, and T. Böhlke, "Fast implicit solvers for phase-field fracture problems on heterogeneous microstructures," *Computer Methods in Applied Mechanics and Engineering*, vol. 363, p. 112793, 2020.

[26] D. Jeulin, "Towards crack paths simulations in media with a random fracture energy," *International Journal of Solids and Structures*, vol. 184, pp. 279–286, 2020.

[27] F. Vicentini, P. Carrara, and L. De Lorenzis, "Phase-field modeling of brittle fracture in heterogeneous bars." https://arxiv.org/abs/2201.02152, 2022.

[28] C. Miehe, "Comparison of two algorithms for the computation of fourth-order isotropic tensor functions," *Computers and Structures*, vol. 66, no. 1, pp. 37–43, 1998.

[29] "AMITEX-FFTP." http://www.maisondelasimulation.fr/projects/amitex/general/_build/html/.

[30] F. Willot, "Fourier-based schemes for computing the mechanical response of composites with accurate local fields," *Comptes Rendus - Mecanique*, vol. 343, no. 3, pp. 232–245, 2015.

[31] M. Kabel, S. Fliegener, and M. Schneider, "Mixed boundary conditions for fft-based homogenization at finite strains," *Computational Mechanics*, vol. 57, pp. 193–210, 2015.

[32] T. Hobbiebrunken, M. Hojo, T. Adachi, C. De Jong, and B. Fiedler, "Evaluation of interfacial strength in CF/epoxies using FEM and in-situ experiments," *Composites Part A: Applied Science and Manufacturing*, vol. 37, no. 12, pp. 2248–2256, 2006.

[33] A. Sharma, S. Daggumati, A. Gupta, and W. Van Paepegem, "On the prediction of the bi-axial failure envelope of a UD CFRP composite lamina using computational micromechanics: Effect of microscale parameters on macroscale stress–strain behavior," *Composite Structures*, vol. 251, p. 112605, 2020.